

M.Sc. Thesis

Myelin Imaging in Brain using Inhomogeneous Magnetization Transfer(ihMT) at 3T and 7T

Manojna Vedula

Abstract

Demyelination is described as loss of myelin sheath in neurons which could lead to disruption in signal transmission in nervous system. Inhomogeneous Magnetization Transfer(ihMT) is a novel MRI technique used to image myelin. It uses the dipolar coupling between methyl chains in lipid layers of myelin to acquire myelin specific information. In this study, we investigated the feasibility of ihMT at 7T. Based on phantom experiments and Bloch simulations, the influence of off-resonance frequency Δ , RF field strength B_1 and RF pulse properties on ihMTR are studied and optimized. For in-vivo imaging, the experiments are conducted on healthy volunteers. Since B_1 inhomogeneities are prevalent at higher fields, an optimized protocol is devised to achieve maximum ihMT effect at 7T. A comparison of 3T and 7T for the off-resonance frequency, RF field strength and pulse properties is presented to emphasize the impact of parameters at both the field strengths.

Myelin Imaging in Brain using Inhomogeneous Magnetization Transfer(ihMT) at 3T and 7T

THESIS

submitted in partial fulfillment of the
requirements for the degree of

MASTER OF SCIENCE

in

ELECTRICAL ENGINEERING

by

Manojna Vedula
born in Vizianagaram, India

This work was performed in:

Circuits and Systems Group
Department of Signals and Systems& Electrical Engineering
Faculty of Electrical Engineering, Mathematics and Computer Science
Delft University of Technology



Delft University of Technology

Copyright © 2020 Circuits and Systems Group
All rights reserved.

DELFT UNIVERSITY OF TECHNOLOGY
DEPARTMENT OF
SIGNALS AND SYSTEMS& ELECTRICAL ENGINEERING

The undersigned hereby certify that they have read and recommend to the Faculty of Electrical Engineering, Mathematics and Computer Science for acceptance a thesis entitled “**Myelin Imaging in Brain using Inhomogeneous Magnetization Transfer(ihMT) at 3T and 7T**” by **Manojna Vedula** in partial fulfillment of the requirements for the degree of **Master of Science**.

Dated: 26-03-2020

Chairman:

prof.dr.ir. R.F. Remis

Advisor:

dr.ir. A.E. Ercan

Committee Members:

prof. dr.ir.M. Staring

Preface

This thesis is written as a part of my masters programme in Electrical Engineering at TU Delft. It is a documentation of my thesis work done from May 2019 to March 2020.

I would like to thank my supervisor at TU Delft, prof.dr.ir.R. Remis who was available every time I needed help and provided me with the required ideas to tackle the problems at hand.

I would like to sincerely thank my daily supervisor at Leiden University Medical Centre dr.ir. A. E. Ercan for her constant guidance and support during the entire duration of my thesis. I am very grateful for all the help and emotional support I received from her in my difficult situations.

I would also like to thank prof.dr.ir. M. Starring for being a part of my committee in these unusual conditions.

I would also like to thank everyone who helped me with my work at LUMC. I also wish to thank my family for their support and guidance during my masters. Finally, I would like to thank my friends in India and from TU Delft for constantly supporting me.

Manojna Vedula
Delft, The Netherlands
26-03-2020

Contents

| | |
|---|-------------|
| Preface | v |
| Abbreviations | xi |
| Nomenclature | xiii |
| 1 Introduction | 1 |
| 1.1 Problem Statement | 1 |
| 1.2 Research question | 2 |
| 1.3 Outline of the report | 2 |
| 2 Background | 5 |
| 2.1 Nervous System | 5 |
| 2.1.1 Myelin | 5 |
| 2.2 Imaging Myelin | 7 |
| 2.3 Magnetization Transfer imaging | 8 |
| 2.3.1 Two pool Model-Liquid pool and Macro-molecular pool | 9 |
| 2.3.2 Quantitative Magnetization Transfer(qMT) | 10 |
| 2.3.3 Disadvantages of Magnetization Transfer | 11 |
| 2.4 inhomogeneous Magnetization Transfer imaging | 11 |
| 2.4.1 Dipolar Coupling | 11 |
| 2.4.2 Modified two pool model | 12 |
| 2.4.3 Bloch-McConnell-Provotorov Equations/ Modified Bloch Equations | 13 |
| 2.4.4 Indirect measure of Myelin: inhomogeneous Magnetization Transfer Ratio(ihMTR) | 15 |
| 2.5 Benefits of Ultra-high fields | 17 |
| 3 Methods | 19 |
| 3.1 Numerical simulations | 19 |
| 3.1.1 Steady state solution for Matrix differential equation | 21 |
| 3.1.2 Euler's method | 21 |
| 3.2 Experimental studies: MRI scan protocol for phantom and in-vivo imaging | 22 |
| 3.2.1 ihMT preparation pulse sequence | 22 |
| 3.2.2 Data Acquisition | 23 |
| 3.2.3 Selection of ROI | 26 |
| 4 Results | 27 |
| 4.1 Simulation Results | 27 |
| 4.2 Experimental results: Phantom and in-vivo imaging | 28 |
| 4.2.1 Acquisition modes | 28 |
| 4.2.2 Influence of off-resonance frequency (Δ) | 29 |

| | | |
|----------|--|-----------|
| 4.2.3 | Influence of Pulse shape | 31 |
| 4.2.4 | Influence of RF field strength (B_1) | 33 |
| 4.2.5 | Influence of number of pulses (N_P) | 35 |
| 4.3 | Optimized protocol for phantom and in-vivo imaging | 37 |
| 5 | Discussion | 39 |
| 6 | Conclusion and Future study | 43 |
| 6.1 | Conclusion | 43 |
| 6.2 | Future work | 43 |
| A | Appendix | 49 |
| A.1 | Phantom results | 49 |

List of Figures

| | | |
|------|--|----|
| 2.1 | Structure of Neuron [1] | 5 |
| 2.2 | Phospholipid bilayers of Myelin [1] | 6 |
| 2.3 | Spectrum of water pool and macro-molecule pool [12] | 7 |
| 2.4 | Interaction between the macro-molecular pool and water pool in the presence of an RF pulse [14]. | 8 |
| 2.5 | Line-shape of the water pool and macro-molecular pool. Bold line shows the initial line-shapes of the pool and dotted line shows the reduction in the longitudinal magnetization of the water pool after applying RF pulse with off-resonance frequency (Δ) [13]. | 9 |
| 2.6 | a. Represents the two pools, free and macro-molecular pool, in absence of RF pulse. b. Represents the two pools when RF is applied at offset frequency and spin exchanges is enabled | 10 |
| 2.7 | Schematic representation of bonds in macro-molecules [18] | 12 |
| 2.8 | a. Represents the two pools when a single RF is applied, emphasizing the impact of dipolar pool in semi-solid pool. b. Represents the two pool model when RF is simultaneously applied at both sides of water frequency with the same frequency offset, showing the decoupled Zeeman and dipolar pools in macro-molecular pool | 13 |
| 2.9 | A. Represents the Cosine modulated dual RF pulses with equal power in positive and negative end of the off-resonance frequency simultaneously B. Represents frequency altering dual RF preparation pulse with an interpulse interval, Δt [31] | 16 |
| 2.10 | pulse sequences for preparation of ihMT | 17 |
| 3.1 | Pulsed ihMT acquisition | 23 |
| 3.2 | Scan planning for in-vivo imaging | 25 |
| 3.3 | Selecting ROI in white matter of human brain | 26 |
| 4.1 | a. B_{1RMS} vs ihMTR b. TR vs ihMTR | 27 |
| 4.2 | Off-resonance frequencies vs ihMTR for 7T parameters using Euler's method | 28 |
| 4.3 | a. Acquisition modes vs ihMTR at 3T b. Acquisition modes vs ihMTR at 7T | 28 |
| 4.4 | A. Phantom scan of one of the 7 slices using EPI for acquisition with geometrical distortion B. Phantom scan using TFE acquisition. | 29 |
| 4.5 | Comparison of off-resonance frequencies vs ihMTR % for different B_1s at 3T and 7T from phantom | 30 |
| 4.6 | Comparison of off-resonance frequencies vs ihMTR % for 3T and 7T from Phantom | 31 |
| 4.7 | Off-set frequency Δ vs ihMTR 3T and 7T from in-vivo human brain | 31 |
| 4.8 | Pulse shapes vs ihMTR at 3T and 7T from phantom | 32 |
| 4.9 | Pulse-shapes vs ihMTR at 3T and 7T from in-vivo human brain | 33 |
| 4.10 | RF strength B_1 vs ihMTR for 3T and 7T from phantom | 34 |

| | | | | | | |
|---------|---|----|--|----|---|----|
| 4.11 a. | B_1 vs ihMTR at 3T and 7T when preparation sequence is composed of 100 hanning pulses from in-vivo human brain. | b. | B_1 vs ihMTR at 3T and 7T when Hyperbolic-secant pulses are used for preparation from in-vivo human brain. | 34 | | |
| 4.12 a. | Number of Pulses vs ihMTR at 3T for different B_1 strengths for Phantom | b. | Number of Pulses vs ihMTR at 7T for different B_1 strengths from phantom | 35 | | |
| 4.13 | Number of Pulses vs ihMTR at 3T and 7T from phantom | | | 36 | | |
| 4.14 a. | N_P vs ihMTR at 3T and 7T when hanning pulse is used for in-vivo human brain. | b. | N_P vs ihMTR at 3T and 7T when hyperbolic-secant is used from in-vivo human brain. | 36 | | |
| 4.15 a. | In-vivo image with optimized protocol at 3T displaying maximum ihMT effect. | | | b. | In-vivo image with optimized protocol at 7T | 37 |
| A.1 | Off-resonance frequencies vs ihMTR for 3T vs 7T | | | 50 | | |
| A.2 | RF strength B_1 vs ihMTR for 3T vs 7T | | | 50 | | |
| A.3 | Repetition time (TR) vs ihMTR for 3T vs 7T | | | 51 | | |
| A.4 | Pulse shapes vs ihMTR for 3T vs 7T | | | 51 | | |

Abbreviations

| | |
|--------------|--|
| CNS | Central Nervous System |
| PNS | Peripheral Nervous System |
| MS | Multiple Sclerosis |
| WM | White Matter |
| GM | Grey Matter |
| MRI | Magnetic Resonance Imaging |
| MT | Magnetization Transfer |
| ihMT | inhomogeneous Magnetization Transfer |
| MBP | Myelin Basic Protein |
| PLP | Proteolipid Protein |
| CNP | Cyclic Nucleotide Phosphodiesterase |
| MAG | Myelin-Associated Glycoprotein |
| MWI | Myelin-Water Imaging |
| DTI | Diffusion Tensor Imaging |
| RF | Radio Frequency |
| FWHM | Full Width Half Maximum |
| CEST | Chemical Exchange Saturation Transfer |
| MTR | Magnetization Transfer Ratio |
| qMT | Quantitative Magnetization Transfer |
| CSF | Cerebrospinal fluid |
| NMR | Nuclear Magnetic Resonance |
| NOE | Nuclear Overhauser Effect |
| ihMTR | Inhomogeneous Magnetization Transfer Ratio |
| SAR | Specific Absorption Rate |
| CW | Continuous Wave |
| PW | Pulsed Wave |
| CM | Cosine Modulated |
| SNR | Signal to Noise Ratio |
| CNR | Contrast to Noise Ratio |
| ROI | Region of Interest |

| | |
|------------|---------------------|
| EPI | Echo Planer Imaging |
| TFE | Turbo Field Echo |
| RMS | Root Mean Square |

Nomenclature

| | |
|----------------------|---|
| T_1 | Longitudinal Relaxation time |
| T_2 | Transverse Relaxation time |
| $M_Z^A(t)$ | Magnetization of water pool as function of time |
| M_0^A | Initial magnetization/spin population of water pool |
| $M_Z^B(t)$ | Magnetization of macro-molecular pool as function of time |
| M_0^B | Initial magnetization/spin population of macro-molecular pool |
| R_{1A} | Longitudinal relaxation rate of water pool |
| R_{1B} | Longitudinal relaxation rate of macro-molecular pool |
| R | Fundamental Rate Constant for spin exchange |
| T_{1D} | Dipolar Relaxation time |
| B_0 | Static magnetic field strength |
| B_1 | RF field strength |
| N_p | Number of pulses |
| D | Local dipolar field |
| Δ | Off-resonance frequency |
| $\beta(t)$ | Inverse dipolar spin temperature |
| R_{RFA} | RF absorption of water pool |
| R_{RFB} | RF absorption of macro-molecular pool |
| TR | Relaxation time |
| TE | Echo time |
| T_{2A} | Transverse magnetization of water pool |
| T_{2B} | Transverse magnetization of macro-molecular pool |
| ω_1 | Amplitude of off-resonance frequency in radians |
| γ | Gyromagnetic ratio |
| θ | Angle between myelin layers and static magnetic field |
| $G_L(2\pi\Delta)$ | Absorption line-shape for Lorentzian |
| $G_G(2\pi\Delta)$ | Absorption line-shape for Gaussian |
| $G_{SL}(2\pi\Delta)$ | Absorption line-shape for Super-Lorentzian |
| s_{MT} | Signal acquired after applying off-resonance frequency |
| s_0 | MR signal without any off-resonance or preparation pulses |

| | |
|-----------|--|
| s_+ | Signal acquired when Single RF pulse is applied at $+\Delta$ |
| s_- | Signal acquired when Single RF pulse is applied at $-\Delta$ |
| s_{\pm} | Signal acquired when dual RF pulse is applied at $\pm\Delta$ |
| s_{\mp} | Signal acquired when dual RF pulse is applied at $\mp\Delta$ |
| PW | Pulse width of the preparation sequence |

1.1 Problem Statement

Myelin, a protein-lipid layer is essential for the depolarisation of membrane and conduction of action potential [1] in nervous system. Any damage to the myelin sheath can result in insufficient concentration of sodium and potassium ions for transfer of electrical signals through the nerve, thereby slowing down the signal transmission in nerve and finally rendering it useless [2].

Demyelination is associated with loss of myelin sheath around axon in the neurons affecting Central Nervous System(CNS) and Peripheral Nervous System(PNS) of the body [2].

Multiple sclerosis (MS) is one of demyelination diseases affecting CNS and is recognized as chronic, disabling neurological disorder. It is caused by an auto-immune reaction whose main pathology is known to be accumulated demyelination and damage to axon. Approximately 2.3 million people are affected by MS and most of them are young adults. Due to disruption in signal transmit between the CNS and muscles, the symptoms can vary from patient to patient. Based on the symptoms, the severity and impact of MS is determined. For example, in the most common type of MS, relapsing-remitting MS, myelin sheath is damaged and repaired multiple times. However, in progressive MS, demyelination leads to neuronal death leading to severe disability [5]. Previously, in most cases the diagnosis is confined to postmortem confirmation. But, with increasing number of demyelination diseases all over the world, accurate evaluation of myelin content is very crucial. MS do not have a cure but the progression of the disease can be restricted with the help of early diagnostics [3].

Imaging myelin is the key feature for detecting demyelination diseases and to monitor the disease progression and therapy efficiency. Magnetic Resonance Imaging (MRI) is a conventional method used imaging neuronal structures for its resolution and contrast enhancement techniques. Most of the MR signal is comprised of protons of the water molecules in the body. Myelin belongs to the macro-molecular pool which normally is not MR visible [4]. Since direct measure of myelin is not a possibility, a lot of indirect methods based on the protons in the macro-molecules and water molecules trapped in lipid layers of myelin are explored. Over the years, many techniques like T_1 weighted imaging, T_2 Relaxometry, Diffusion Tensor Imaging(DTI) and Myelin Water imaging(MWI) are used in myelin imaging [5].

Magnetization Transfer(MT) imaging is one such technique which uses a tuned

Radio Frequency(RF) pulse prior to MR acquisition to make magnetization from the trapped protons in the macro-molecules MR visible. RF pulse saturates the macro-molecules to obtain information from them via exchange of protons between the water and macro-molecules [6]. But MT signal is not a good measure of demyelination due to its lack of specificity to myelin [7].

Inhomogeneous Magnetization Transfer(ihMT) imaging is a novel MRI technique which is an extension of MT concept. It considers the chemical and structural information of myelin and can be used for myelin specific imaging [8]. Till now, there is no validation of ihMT technique in detection of demyelination diseases. However, in recent years due to increase in MS cases, the implementation of ihMT is given great deal of attention. In this research, ihMT technique is evaluated with the help of numerical simulations, phantom and in-vivo experiments.

1.2 Research question

To date, most of the ihMT implementation in human brain is confined to lower magnetic fields with field strength $B_0=1.5$ Tesla[7, 35] and few studies extended to 3T[19, 20, 26, 32]. Ultra-high fields with strength $B_0=11.75$ are used in imaging mouse central nervous system [31, 33]. Although clinically not implemented, there is significant increase in research on 7T scanners. In this research, the objective is to implement ihMT at 7T. Results are compared to that of clinical 3T scanner results.

Since ihMTR is an interplay of various parameters involved in preparation and acquisition stages, the aim is to investigate all the parameters influencing ihMT at both field strengths and propose the best protocol to observe maximum ihMT effect. This forms a basis for the following research questions.

- Is ihMT feasible at 7T?
- What is the range of RF pulse frequency to target the H-H bond in lipid layers to obtain maximum myelin specific data at 3T and 7T?
- What is the optimum RF field strength B_1 to be applied following SAR limitations?
- What are the pulse shape and number of pulses to be used in the preparation sequence to obtain the maximum ihMTR?

1.3 Outline of the report

The report is divided into six chapters. Chapter 2 presents the background study for the thesis. In chapter 2, structure of the neuron is demonstrated and a short explanation of functional and structural aspects of myelin is presented. A brief account of chemical composition of myelin is also given. Complications involved in non-invasive

imaging of myelin are discussed with the help of water and macro-molecular pools in the biological systems. Also, in chapter 2, the theory of MT and ihMT is explained. The modified Bloch equations and dipolar coupling effect in ihMT are emphasized. Finally, benefits and pitfalls of ultra-high fields, in general and with respect to MS are discussed.

In chapter 3 the methodologies used for numerical simulations of ihMT and MRI protocols implemented in the experimental studies of phantom and in-vivo imaging of human brain are presented. Parameters and the protocol used for its study using simulations, phantom and in-vivo experiments are tabulated.

Chapter 4 illustrates the results obtained and shows the impact of the preparation and acquisition parameters on ihMT. The optimized protocols for phantom and in-vivo at 3T and 7T are presented.

Chapter 5 discusses all the inferences from the results. A comparison of current work to existing literature for each parameter is done to evaluate the accuracy of the results and to present significant contributions of this study. Finally, a short summary followed by the major findings of the work and recommendations for future work are given in chapter 6.

Background

2.1 Nervous System

Nervous system in humans is categorized into CNS and PNS. PNS collects information from the internal and external sources and is responsible for the motor and sensory neurons. They act as link between brain and sensory organs. While CNS integrates all the information. It consists of two main parts: Brain and Spinal cord. Apart from their functional dissimilarities, CNS and PNS have micro-structural differences in the cells.

CNS has Grey Matter(GM) and White Matter(WM). White matter tissue contains myelinated axons, glial cells, and capillaries. The pale appearance is due to the lipids in myelin. While GM consists of neuronal dendrites, cell bodies, glial cells, and capillaries. It is darker due to the relatively low myelin content [1].

Neurons are the most important part of the nervous system. With the support of glial cells, helper cells in nervous system, they perform all the functions. Neurons are responsible for the transfer of synaptic response. They coordinate the data transfers from muscle, sensory organs to brain and vice-versa. The myelinated segments of the axons are around 150 milli-metres in length and are only interrupted by small gaps, the nodes of Ranvier, which contain sodium channels at a high density. The basic structure of a (myelinated) neuron is shown in Figure 2.1

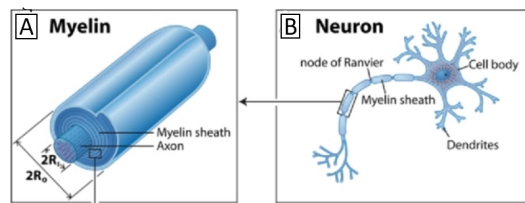


Figure 2.1: Structure of Neuron [1]

2.1.1 Myelin

Myelin is a critical feature of nervous system and accounts for 14 % of the wet mass of WM. It is a lipid-protein bilayer that extends from the outer membrane of glial cells and discretely winds around individual axon, resulting in the speedy transfer of electric signal. It is formed in the CNS by glial cells called oligodendrocytes, and in the PNS by glial cells called Schwann cells [2].

2.1.1.1 Functions of Myelin

The foremost function of myelin is to increase the conduction speed in the neurons. In unmyelinated neurons, the action potential travels along the length of the axon and is transferred from one neuron to other. However, in myelinated neurons, most of the axon is covered with multiple blocks of myelin sheath with nodes of Ranvier in between. Myelin sheath lacks voltage-gated sodium channels rendering it incompetent for transferring action potential. With the presence of myelin sheath, the action potential hops in between the nodes which are only points containing sodium channels throughout the axon, ensuring faster conduction. This type of conduction of action potential is defined as saltatory conduction [2]. Apart from acting as insulator, it provides strength to the axon.

2.1.1.2 Chemical Composition of Myelin

Myelin sheath is comprised of 40% of water, while the lipid content is around 60-70% and proteins are between 15-25%. Myelin is comprised of different proteins in CNS and PNS but the most repetitive ones are myelin basic protein (MBP), proteolipid protein (PLP), cyclic nucleotide phosphodiesterase (CNP) and myelin-associated glycoprotein (MAG) as shown in Figure 2.2[1].

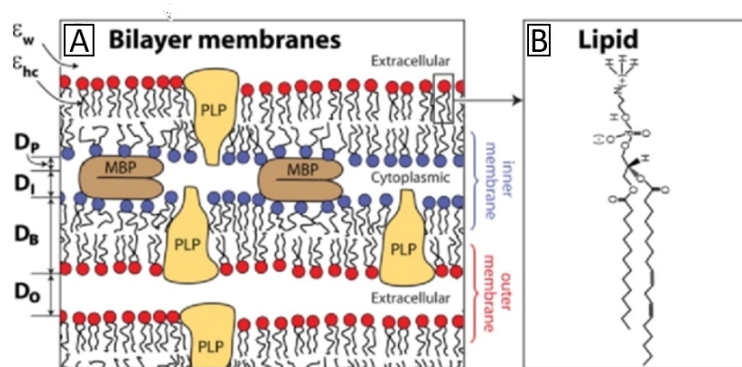


Figure 2.2: Phospholipid bilayers of Myelin [1]

Myelin is spread as multiple blocks of double bi-layers separated by 3-4 nm thick aqueous layers that alternate between the cytoplasmic and extracellular faces of cell membranes. MBP which is 20–30% of total protein by weight, is located only between the 2 cytoplasmic faces and acts as an inter-membrane adhesion protein [1].

Multiple lipids make up the myelin sheath and each sheath has its own distinct physical properties, contributes to the structure and possibly the pathogenesis of the myelin membrane. The asymmetric distribution of lipid composition on the cytoplasmic and extracellular faces likely also plays an important role [2].

2.1.1.3 Demyelination

If myelin sheath is damaged, the axon is not insulated anymore but it does not have adequate concentration of sodium, potassium, and other ionic channels [9]. It leads to disturbance in hopping of action potential in between Nodes of Ranvier. The irregular concentration of ions in non-insulated areas of axon disrupts sufficient flow of ions to cause depolarization. Due to its inability to transfer action potential, nerve is rendered useless or dead. Loss of myelin sheath can result in disruption in the signal transmission to motor and sensory nerves. Demyelination can be caused due to several CNS diseases such as stroke, spinal cord damage, and MS [5].

2.2 Imaging Myelin

In biological systems, the 1H atoms are present in both aqueous and non-aqueous systems. Aqueous system constitutes the water pool which occupies approximately 70% of the body, while non-aqueous molecules consist of macro-molecules like lipids, carbohydrates, proteins and various nucleic acids. These two spin systems are often referred as free pool for water/aqueous protons and rigid pool for macro-molecules due to their motion in the body. Signals obtained by the conventional MRI are mostly comprised of different T_2 relaxation of protons of water pool. Even though there are significant protons in macro-molecules, they do not contribute to MR signal. To understand the problems in imaging macro-molecular pool, mainly myelin, the spectral properties of the pools are referred to [10].

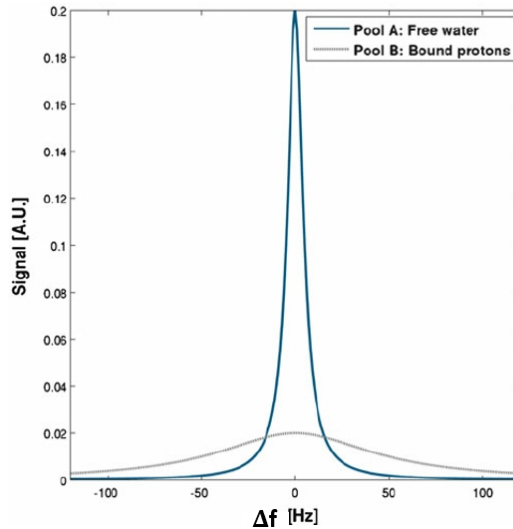


Figure 2.3: Spectrum of water pool and macro-molecule pool [12]

The spectrum of water and macro-molecular pools are shown in Figure 2.3. The spectral width and T_2 are inter-related. Full Width Half Maximum(FWHM) define the line width of a spectrum. Water pool in biological systems usually have Lorentzian

line-shape and FWHM is defined as $\frac{1}{\pi T_2}$. Macro-molecules with broader spectrum have significantly lower T_2 , while the water protons have very narrow line-shape consequently resulting in higher T_2 .

Water has the central frequency close to 0 Hz and T_2 is in the order of milliseconds(ms). Macro-molecules spectrum is spread in some KHz range and T_2 is estimated to be in the order of micro-seconds(μs). However, coupling between the macro-molecule pool and water enables exchange of spins between both pools.

Due to their broad spectral width, macro-molecular pools are (approximately 10^6 times) prone to be responsive to off-resonance irradiation. When a RF pulse is applied, it saturates the magnetization of macro-molecules which is transferred to free pool protons with spin exchange. This exchange process depends on various factors like initial number of spins in both the pools, exchange rate, and line shape of the pools. This forms bases for the Magnetization Transfer(MT) technique, which is explained in next section [11].

2.3 Magnetization Transfer imaging

Magnetization Transfer(MT) is based on the interaction/exchange process between protons in the water and the protons in macro-molecules. The concept of MT is intertwined with the physio-chemical exchange of protons between the pools and molecular motion in the rigid pool [12]. In 1963, Forsén and Hoffman used saturation transfer technique to calculate the exchange rate of a chemical reaction. But the first in-vivo implementation of magnetization transfer is done by Wolf and Balaban in 1989. They discovered MT while trying to image urea and observed a huge contrast in the image [14]. It reflects the change in contrast of different tissues based on the macro-molecular content.

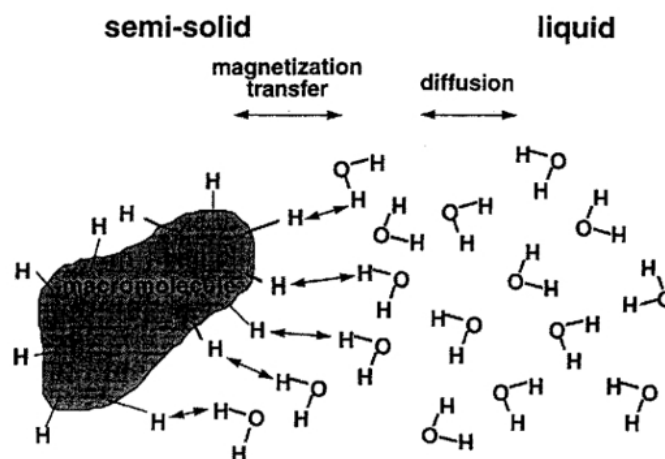


Figure 2.4: Interaction between the macro-molecular pool and water pool in the presence of an RF pulse [14].

MT is the selective imaging of macro-molecules based on saturation exchange between the protons of macro-molecules and water pool. The saturation exchange between the pools could be the result of three processes: dipole-dipole interactions between protons, exchange of protons between water and macro-molecules and Chemical exchange Saturation Transfer(CEST). In MT, the saturation exchange originates from saturated protons of macro-molecules to the protons of water pool [15, 16]. By applying MT pulse, the available longitudinal magnetization M_Z is reduced for water pool. This can be observed in Figure 2.5.

In absence of any preparation pulse, the acquisition resembles the conventional MRI acquisition with signal comprised of magnetization from water pool. When a preparation pulse is applied prior to acquisition with an off-resonance frequency which is far from the water frequency, MT effect is observed. As a result, the protons in the macro-molecules are saturated. The saturated protons are exchanged with the protons of water pool resulting in change of spin population in both pools. Due to spin interchange, protons of macro-molecular pool are now in water pool which is MR visible. The saturation exchange in terms of spin population and rate of transfer is explained using two pool model [11].

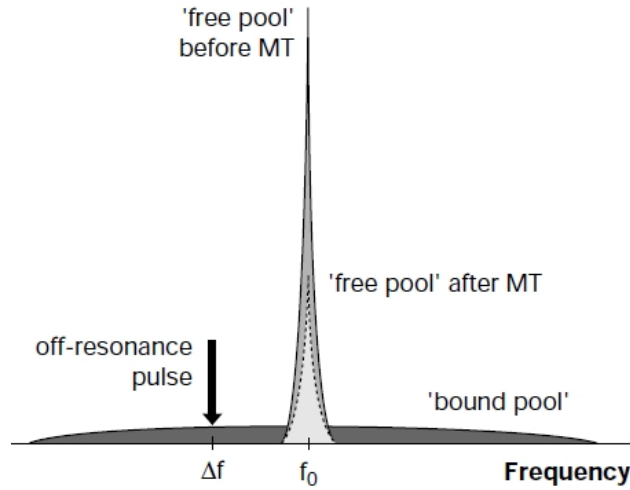


Figure 2.5: Line-shape of the water pool and macro-molecular pool. Bold line shows the initial line-shapes of the pool and dotted line shows the reduction in the longitudinal magnetization of the water pool after applying RF pulse with off-resonance frequency (Δ) [13].

2.3.1 Two pool Model-Liquid pool and Macro-molecular pool

The two pool model is the simplest and most extensively used MT tissue model. Protons are considered to be either in a highly mobile liquid pool (water) or in a semi-solid macro-molecular pool of relatively restricted motion. In this model, free pool is referred as pool A and macro-molecular as pool B. The spin population in liquid pool (Pool A) is represented by M_Z^A while in macro-molecular pool M_Z^B while

the initial spin populations are M_0^A and M_0^B respectively. The available protons/spin population of Pool A is significantly higher compared to macro-molecular pool in absence of RF pulse, as depicted in Figure 2.7. The longitudinal relaxation rate of pool A and B, given as R_{1A} and R_{1B} , are responsible for the recovery of longitudinal magnetization of the pools.

In the absence of the RF pulse, the magnetization is solely contributed by the Pool A due to the abundance. After applying RF pulse, a link is established between the pools and now there is spin exchange due to saturation. The fundamental rate constant (R) determines the rate of transfer of spins between the pools. Now the signal acquired will include the saturated protons signal from the macro-molecular pool as well [6].

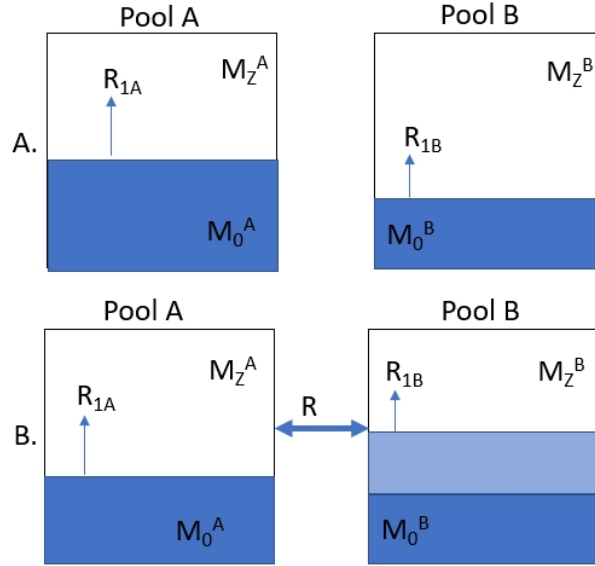


Figure 2.6: a. Represents the two pools, free and macro-molecular pool, in absence of RF pulse. b. Represents the two pools when RF is applied at offset frequency and spin exchanges is enabled

The magnitude of this MT effect can be quantified by obtaining two sets of images (one with an RF pulse and one without it) and then digitally subtracting them. Magnetization Transfer Ratio (MTR) is given as

$$MTR = 1 - s_{MT}/s_0 \quad (2.1)$$

where s_0 is the magnitude of signal without the MT pulse s_{MT} is the signal after the MT pulse has been applied [17].

2.3.2 Quantitative Magnetization Transfer(qMT)

Many studies established a connection between the size of the macro-molecular pool and MTR. Implementing a quantitative study of MT can improve the results of classical

approach. Various off-resonance frequencies and RF field strengths can be applied to sensitize various sections of macro-molecular pool. These studies help in framing a model to estimate the pool size and properties [3, 18].

2.3.3 Disadvantages of Magnetization Transfer

MT is known to occur in biological tissues comprised of substantial amount of liquid pool and macro-molecular pool. Studies show that MTR is high in WM, low in GM and null in CSF. Despite the above argument, it cannot be used in detection of myelin. As MT effect is a combined signal from various proteins and other macro-molecules, it provides information about the macro-molecules in brain. Hence it cannot deliver the required specificity for myelin [4].

2.4 inhomogeneous Magnetization Transfer imaging

Inhomogeneous Magnetization Transfer(ihMT), an extension of MT technique, effectively utilizes the information of residual dipolar coupling between the lipid layers of myelin. The subtraction of signal acquired from dual and single RF preparation pulse is the unique methodology which sets it apart from MT and other MRI contrast enhancing techniques [19, 20].

2.4.1 Dipolar Coupling

Over the last two decades, 1H NMR has been an important method for investigating the structure and dynamics of liquid crystalline systems such as lipid bi-layers. Typically, in liquid systems, the interactions between the molecules are averaged out due to the rapid orientation changes in the molecule. But in motion restricted systems, like semi-solid pools in biological systems, this would not be the case. Since the motion restricted protons cannot move rapidly, all the interactions are not cancelled out and can result in residual dipolar coupling. Lately, this information has been the interest of study as this can provide an in-depth structural analysis of proteins.

Previously, for determining structural information, Nuclear Overhauser Effect(NOE) contacts between the nuclei are analysed as they provide the distance details. However, residual dipolar coupling, observed in hetronuclear systems like C-H connected by single bond or homonuclear systems like H-H provide special information for structural determination [21].

A basic protein structure is shown in Figure 2.7. The desirable range of off-resonance frequency to tune the dipolar coupling between various bond is varied. H-H bonds are known to exhibit coupling around 10-22 kHz.

Myelin composition is majorly influenced by the lipids and proteolipid proteins. Along with the hydrophobic nature of lipids and proteins, the inter-molecular attraction between the lipids are responsible for the densely packed structure myelin sheath. One

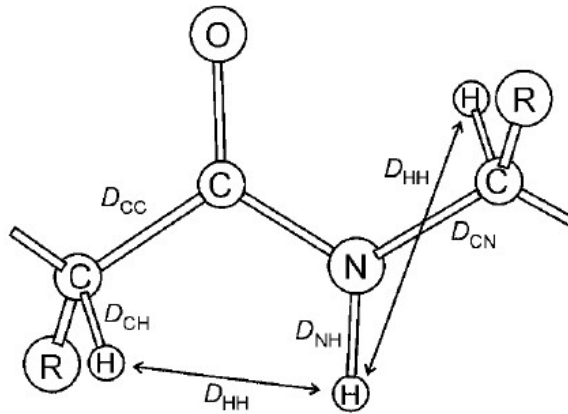


Figure 2.7: Schematic representation of bonds in macro-molecules [18]

of major attractive forces in the myelin is H-H bonds formed by the amide and hydroxyl groups of lipids with water. The most important attractive forces in myelin which are responsible for ihMT effect are the Van der Waals attraction forces between methyl groups of lipid layers. Almost 20% of hydrocarbons in myelin have more than 18 carbon chains. Due to the long hydro-carbon chains, fatty acids in myelin and their additive nature contribute to the strong dipolar coupling [22].

2.4.2 Modified two pool model

The Provotorov theory establishes the basic principle of ihMT [26]. When a RF preparation pulse is applied nearly 7-10 kHz away from the water frequency, the protons present in the macro-molecular pool are saturated, the saturated protons are exchanged with the water protons and a link is established between the residual dipolar pool and Zeeman pool of the macro-molecular pool. The spin population of acquired signal include the saturation exchange between the Zeeman pools of water and macro-molecular pool and also the non-averaged dipolar interactions of the hydrogen atoms in the $-CH_2$ (methylene groups) in the lipid layers.

However, when RF pulse of equal power is applied at both positive and negative end of off-resonance frequency, the residual couplings are cancelled out due to counter balance of dipolar interactions at both ends of off-resonance frequency. The acquired signal would result in only the Zeeman pool interactions of water and macro-molecular pools. The difference between signals acquired with single RF and dual RF will provide the exclusive information from dipolar coupling within the lipid layers of myelin. The difference removes the signal acquired from other components of macro-molecular pool which makes it myelin specific [23, 24]. This phenomenon can be explained using the modified 2 pool model shown in Figure 2.8.

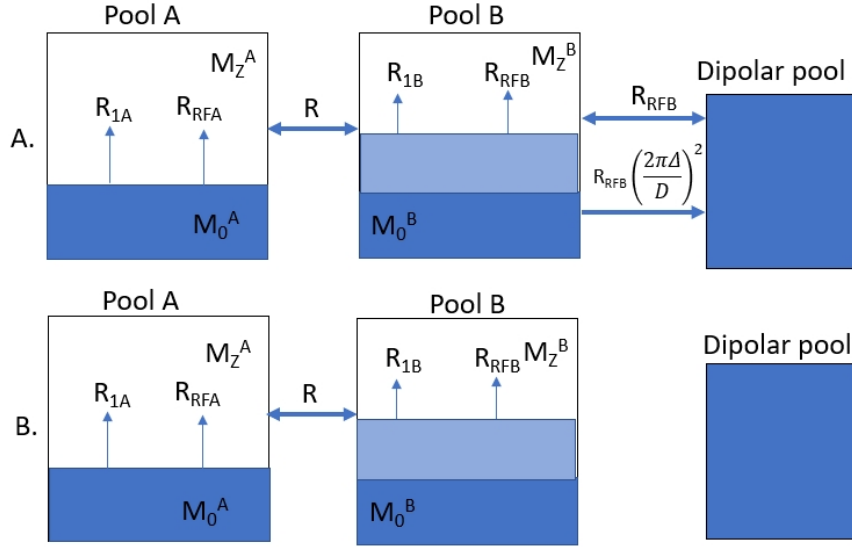


Figure 2.8: a. Represents the two pools when a single RF is applied, emphasizing the impact of dipolar pool in semi-solid pool. b. Represents the two pool model when RF is simultaneously applied at both sides of water frequency with the same frequency offset, showing the decoupled Zeeman and dipolar pools in macro-molecular pool

2.4.3 Bloch-McConnell-Provotorov Equations/ Modified Bloch Equations

Modified Bloch equations express the magnetization of the two pools when a static magnetic field and RF irradiation is applied. They provide the mathematical expression for effect of various parameters on transfer of magnetization in the spin system. The Single RF irradiation effects on the pool magnetization are observed in the following equations [25, 26].

$$dM_Z^A/dt = R_{1A}[M_0^A - M_Z^A(t)] - RM_0^B M_Z^A(t) + RM_0^A M_Z^B(t) - R_{RFA} M_Z^A(t)$$

$$dM_Z^B/dt = R_{1B}[M_0^B - M_Z^B(t)] - RM_0^A M_Z^B(t) + RM_0^B M_Z^A(t) - R_{RFB} M_Z^B(t) + R_{RFB} \beta(t)$$

$$d\beta(t)/dt = \frac{-1}{T_{1D}} \beta(t) + R_{RFB} \left(\frac{2\pi\Delta}{D^2}\right) M_Z^B(t) - R_{RFB} \left(\frac{2\pi\Delta}{D}\right)^2 \beta(t)$$

In the equations, the magnetization of pool A is affected by longitudinal magnetization, rate of exchange of spins between the pools and the absorption line-shape of the pool. While for the pool B, along with these components, dipolar pool also impacts the magnetization. While, for the dual RF there is no dipolar component affecting the magnetization of either pools which can be observed in the equations below [24, 26].

$$dM_Z^A/dt = R_{1A}[M_0^A - M_Z^A(t)] - RM_0^B M_Z^A(t) + RM_0^A M_Z^B(t) - R_{RFA} M_Z^A(t)$$

$$dM_Z^B/dt = R_{1B}[M_0^B - M_Z^B(t)] - RM_0^A M_Z^B(t) + RM_0^B M_Z^A(t) - R_{RFB} M_Z^B(t)$$

Here the M_Z^A and M_Z^B are the longitudinal magnetization of the free pool and semi-solid pool as a function of time, as they vary depending on various parameters. M_0^A and M_0^B are the longitudinal magnetization or spin populations at equilibrium i.e., before applying RF pre-pulses. R is the fundamental rate constant describing the saturation exchange between the two pools. D is the local dipolar field.

The amount of signal acquired depends on the rate of exchange of spin population along with initial fraction of the pools. It is observed that larger the semi-solid pool fraction, higher the ihMT signal acquisition as more residual dipolar content from the lipid layers is impacting the magnetization. R_{1A} and R_{1B} are rates of longitudinal magnetization rates of free and macro-molecular pools respectively.

The dipolar pool is represented by the dipolar relaxation time T_{1D} and the dipolar spin temperature β where $\beta' = 2\pi\Delta\beta$. The ihMT signal is majorly influenced by the offset frequency at which the pre-pulse is applied, here Δ represents the offset frequency. R_{RFA} and R_{RFB} are the absorption terms of the pools and depend on the line-shape. The general formula for calculating R_{RFA} and R_{RFB} is given by equation 3.1.

$$R_{RFi} = \omega_1^2 \pi g_i (2\pi\Delta) \quad (2.2)$$

Where ω_1 is defined as amplitude of the off resonance frequency in radians ($\omega_1 = 2\pi\gamma B_1$). It is dependent on the RF field strength in micro-Tesla B_1 and the gyromagnetic ratio (γ) which is ratio of its magnetic moment to its angular momentum. In the case of 1H , the gyromagnetic ratio is 42.58 MHz per Tesla [27]. $g_i(2\pi\Delta)$ is the absorption line-shape.

Many researchers examined the possible absorption line-shapes for the liquid systems and semi-solids. Lorentzian line-shape is widely considered for the aqueous protons, as it is mostly associated with the systems with zero averaged spin interactions. The mathematical representation of the Lorentzian line-shape is expressed in equation 3.1

$$g_L(2\pi\Delta) = \frac{T_{2A}}{\pi} \frac{1}{(1 + (2\pi\Delta T_{2A})^2)} \quad (2.3)$$

In the case of semi-solid/rigid pool, Gaussian and super-Lorentzian are famous choices. Gaussian line-shape is prevalent with motion restricted systems with non-zero dipolar interactions. Few of the researchers considered Gaussian shape for the semi-solid pool but experimental results for various biological tissues like lipids has shown potential inclination towards the Super-Lorentzian line-shape. Refer equation 2.4 for

Gaussian line-shape.

$$g_G(2\pi\Delta) = \frac{T_{2B}}{\sqrt{2\pi}} e^{-(2\pi\Delta T_{2B})^2/2} \quad (2.4)$$

Gaussian line-shape is computationally cheaper as it assumes the myelin lipid layers are parallel to the applied magnetic field. This assumption is inaccurate since the myelin sheath is wound around the axon and assumes angles between 0 to $\pi/2$. Super-Lorentzian ensures the integration of dipolar interactions from all possible angles [29]. The line equation for Super-Lorentzian can be observed in 2.5. When the angle θ is zero, line-shape is same as Gaussian [28].

$$g_{SL}(2\pi\Delta) = \int_0^{\pi/2} \sin\theta d\theta * \sqrt{\frac{2}{\pi}} \frac{T_{2B}}{|3\cos^2\theta - 1|} e^{-2(2\pi\Delta T_{2B}/|3\cos^2\theta - 1|)^2} \quad (2.5)$$

The dipolar field D is calculated as $\frac{1}{\sqrt{15}T_{2B}}$ for super-lorentzian and $\frac{1}{\sqrt{3}T_{2B}}$ for gaussian.

2.4.4 Indirect measure of Myelin: inhomogeneous Magnetization Transfer Ratio(ihMTR)

A typical ihMT implementation can be explained in three parts, ihMT Preparation sequence with RF pulses, image acquisition and calculation of ihMTR for selected a region. Detailed explanation of procedure involved in each part of ihMT and impact of it on ihMTR is discussed in this section.

2.4.4.1 Types of Preparation pulses

ihMT preparation is achieved with the help of either a continuous wave(CW) or Pulsed wave. CW was the first one to be implemented in the tissue and provides the cleanest separation between the amount of saturation in the two pools. It applies a single rectangular pulse, which is sine-modulated in the case of the S_{dual} experiment. Despite the advantages, it is confined to only research purposes because of the Specific Absorption Rate(SAR) limitations.

In CW method, there is a continuous application of RF energy for a long time which could result in heating the subject in clinical imaging. Pulsed MT uses a different technique to apply RF pulse which makes it feasible in practical imaging. It selectively saturates by applying RF pulse at offset frequency. The preparation sequence consists of a train of shaped pulses typically Hann or Gaussian [30]. Pulsed wave is used for single and dual RF preparation pulses.

2.4.4.2 Dual Frequency generation

The dual frequency RF pulse can be generated using two methods, A. Cosine Modulated(CM) pulses and B. Frequency alternating pulses. In the first case, the positive and negative components of RF pulse are applied in sync. This results

in cancellation of any anisotropic residual components and ensures simultaneous saturation on both ends of the frequency bands. CM pulse decouples the Zeeman pool with residual dipolar pool resulting in maximum signal difference between single RF pulse acquisition and dual RF pulse [31]. The CM pulse is shown in Figure 2.9.A.

In alternating frequency pulses, the positive and negative offset frequencies are applied as consecutive pulses in an alternating fashion in the dual pulse. In this procedure, the dipolar and Zeeman pools are not effectively decoupled due to the time gap in the application of positive and negative frequency offset. ihMT signal strength is relatively less compared to cosine modulated. This method also introduces new degree of freedom, switching time (Δt). Switching time is defined as the time difference between consecutive pulses [31].

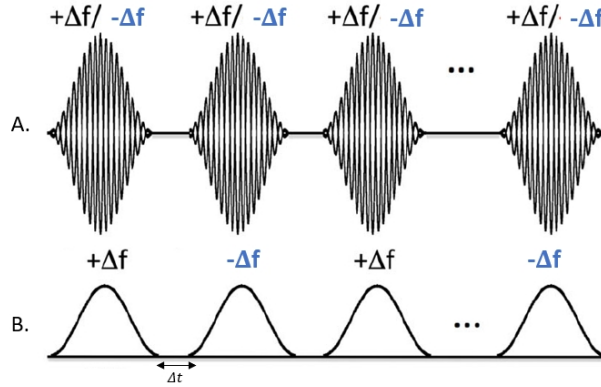


Figure 2.9: A. Represents the Cosine modulated dual RF pulses with equal power in positive and negative end of the off-resonance frequency simultaneously B. Represents frequency altering dual RF preparation pulse with an interpulse interval, Δt [31]

2.4.4.3 Inhomogeneous Magnetization Transfer Ratio(ihMTR)

After applying preparation pulses, each time we acquire an image. For calculating the ihMTR and quantifying the myelin content, five images are to be acquired.

- s_+ represents the acquired information when positive off-resonance RF pulse $+\Delta f$ is used as preparation sequence.
- s_- when RF pulse is applied at the negative end of the same frequency $-\Delta f$.
- For dual frequency RF pulses, s_{\pm} alternating positive and negative RF pulses are applied at the same off-resonance frequency $\pm\Delta f$.
- s_{\mp} for alternating negative and positive RF pulses are applied at the same off-resonance frequency $\mp\Delta f$.
- s_0 signal acquired without any ihMT preparation.

ihMTR calculations can be made with just three images as well, one with single off-resonance frequency, other with dual off-resonance and one without any saturation. The signal is measured at both positive and negative end of the off-resonance frequency to avoid any asymmetrical effects on the line-spectrum due to saturation. The same is applied for dual frequency and averaged in the ihMTR calculations.

$$]ihMTR = \frac{s_+ + s_- - s_{\pm} - s_{\mp}}{2s_0} \quad (2.6)$$

A rectangular pulse with mentioned sequence models for ihMT calculations is shown in figure 2.10.

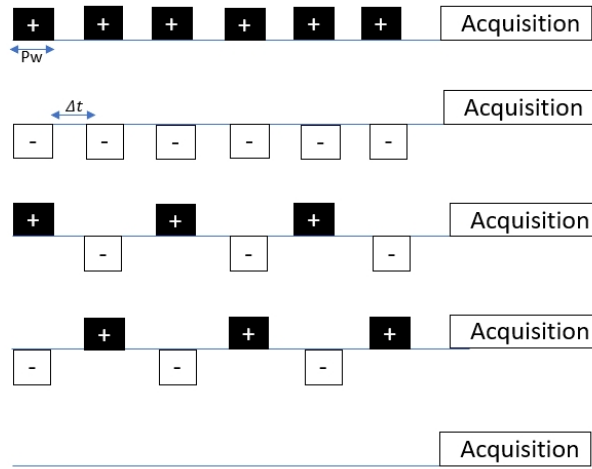


Figure 2.10: pulse sequences for preparation of ihMT

ihMTR depends on various parameters other than myelin content such as off-resonance frequency, RF field strength, dipolar relaxation time T_{1D} and others [32]. The impact of each parameter is studied in discussed in results section.

2.5 Benefits of Ultra-high fields

In recent times, ultra-high field MRI had widely developed and offers a lot of advantages in imaging finer neuronal structures. There is a significant increase in signal to noise ratio(SNR) and contrast to noise ratio(CNR). The increase in SNR can be invested improving spatial resolution or reducing scan time. Additionally, with ultra-high fields, some of the imaging techniques can experience considerable improvement in contrast mechanisms[33].

At 7T, due to higher resolution, there could be improvement in many clinical applications. MS is one of the most important pathologies where 7T importance is stressed on. White matter lesions are considered one of potential indication of

MS. Even though lesions can be imaged at lower field strengths, cortical lesions are challenging to image at such lower resolution. Switching to 7T will improve the spatial resolution and SNR which can provide better visualization of lesions [34].

Even though SNR is very crucial in imaging, Contrast to Noise Ratio(CNR) is very crucial in imaging associated with pathology detection. T_1 -values for grey and white matter increase from 1.5 T to 7 T which can also contribute to imaging at 7T [33].

Table 2.1: Table 2.1: T_1 values for white matter and grey matter at 1.5, 3 and 7T magnetic field strengths

| $B_0(T)/T_1(ms)$ | WM | GM |
|------------------|---------|----------|
| 1.5T | 646±32 | 1197±134 |
| 3T | 838±50 | 1607±112 |
| 7T | 1126±97 | 1939±149 |

Despite these advantages, 7T also has a lot of pitfalls including a range of imaging artifacts and severe inhomogeneity in B_0 and B_1 fields. Due to the B_0 and B_1 inhomogeneity, SNR would be spatially varying. Based on the pulse sequence used, there could be variation of contrast in different locations of image. Apart from imaging complications, 7T introduces some system restrictions in the scanner and patient/subject safety issues. The global SAR is directly proportional to approximately the square of the magnetic field strength. Due to the B_1 inhomogeneities, there is great variation in SAR distribution in brain. Since there could be peaks in SAR at specific locations of the brain, thereby imposing strict limitations on applied pulse sequence. Also, due to the increased field, power deposition on subject while imaging is increased. This could lead to unwanted heating of tissues in the body [34, 35].

Fast imaging techniques and convenient RF pulse shapes could mitigate these limitations. With the help of advanced imaging methods, high tissue sensitivity and high-resolution whole brain imaging can be achieved within a short time frame.

The effect of the parameters on the ihMT is assessed based on the numerical simulations and results of phantom and in-vivo experiments conducted on MRI scanner of field strength $B_0=3\text{T}$ and 7T .

3.1 Numerical simulations

The Bloch-McConnell-Pravotorov equations of the tissue model are expressed as matrix differential equations. Longitudinal magnetization of water and macro-molecular pools for single and dual RF pulses are expressed separately as first-order matrix differential equations and solved using MATLAB (R2019a, MathWorks Inc., Natick, MA, USA).

As discussed in section 2.4.3, modified Bloch equations provide an assessment of impact of various parameters on longitudinal magnetization of both pools. When shaped RF pulses are applied at positive and negative off-resonance frequency ($+\Delta$ or $-\Delta$), it can be observed that M_Z^A , at any instant is dependent on recovery of longitudinal magnetization of pool A with respect to initial spin population, rate of exchange of spins between two pools and direct saturation of the pool A. Now, M_Z^B at any particular time is influenced by the recovery of longitudinal magnetization of pool B, rate of spin exchange between pools, direct saturation of pool B depending on the line-shape and the residual dipolar coupling. The residual dipolar coupling is defined by inverse spin temperature β and dipolar relaxation time which is expressed in the equations.

Initial value of β i.e., prior to the application of preparation sequence, is considered to be zero to specify the non-existence of residual dipolar coupling in macro-molecular in absence of RF fields. Once, preparation sequence is applied, change in β indicates the change in the spin system of pool B and impact of it on the spin population of pools.

$$dM_Z^A/dt = R_{1A}[M_0^A - M_Z^A(t)] - RM_0^B M_Z^A(t) + RM_0^A M_Z^B(t) - R_{RFA} M_Z^A(t)$$

$$dM_Z^B/dt = R_{1B}[M_0^B - M_Z^B(t)] - RM_0^A M_Z^B(t) + RM_0^B M_Z^A(t) - R_{RFB} M_Z^B(t) + 2\pi\Delta R_{RFB} \beta(t)$$

$$d\beta(t)/dt = \frac{-1}{T_{1D}} \beta(t) + R_{RFB} \left(\frac{2\pi\Delta}{D^2}\right) M_Z^B(t) - R_{RFB} \left(\frac{2\pi\Delta}{D}\right)^2 \beta(t)$$

The equations are written in form of matrix differential equation $\frac{dM_S}{dt} = AM_S + B$ [35].

$$\text{Where } M_S = \begin{bmatrix} M_z^A(t) \\ M_z^B(t) \\ \beta(t) \end{bmatrix}$$

$$A = \begin{bmatrix} -(R_{1A} + RM_0^B + R_{RFA}) & RM_0^A & 0 \\ RM_0^B & -(R_{1B} + RM_0^A + R_{RFB}) & 2\pi\Delta R_{RFB} \\ 0 & R_{RFB}(\frac{2\pi\Delta}{D}) & \frac{-1}{T_{1D}} - R_{RFB}(\frac{2\pi\Delta}{D})^2 \end{bmatrix}$$

$$B = \begin{bmatrix} R_{1A}M_0^A \\ R_{1B}M_0^B \\ 0 \end{bmatrix}$$

When dual RF pulses are applied, it can be observed that the dipolar component is averaged to zero and has no impact on longitudinal magnetization of the pools. The matrix representation of the Bloch equations is given below.

$$dM_Z^A/dt = R_{1A}[M_0^A - M_Z^A(t)] - RM_0^B M_Z^A(t) + RM_0^A M_Z^B(t) - R_{RFA}M_Z^A(t)$$

$$dM_Z^B/dt = R_{1B}[M_0^B - M_Z^B(t)] - RM_0^A M_Z^B(t) + RM_0^B M_Z^A(t) - R_{RFB}M_Z^B(t)$$

$$\text{Where } M_D = \begin{bmatrix} M_z^A(t) \\ M_z^B(t) \end{bmatrix}$$

$$E = \begin{bmatrix} -(R_{1A} + RM_0^B + R_{RFA}) & RM_0^A \\ RM_0^B & -(R_{1B} + RM_0^A + R_{RFB}) \end{bmatrix}$$

$$F = \begin{bmatrix} R_{1A}M_0^A \\ R_{1B}M_0^B \end{bmatrix}$$

However, in reality, it depends on the technique used in generation of dual RF pulses. CM RF pulses can effectively decouple the residual pool and Zeeman pools of macro-molecular pool, however alternating $\pm \Delta$ RF pulses do not effectively decouple since there is a time lapse between the $+\Delta$ and $-\Delta$ of RF pulse. There would still be an impact of dipolar coupling on longitudinal magnetization of the pools.

Parameters: Values used for the simulations are based on the estimated parameters for WM in human brain. Since, this study mainly focused on investigating the feasibility of ihMT at 7T, T_1 values for the pools are given accordingly. Longitudinal relaxation rate of pools R_{1A} and R_{1B} are set as 1.1 s^{-1} and 1 s^{-1} respectively. Rate constant for spin exchange is taken as 31 s^{-1} [26]. The initial spin population of the macro-molecular pool is approximated to 13.87% of the water pool while the water pool initial magnetization is normalized to 1 due to the abundance of 1H protons in body.

For simulations, line-shapes of the water pool and macro-molecular pool are considered to be Lorentzian and Gaussian respectively. Despite Super-Lorentzian’s accurate representation of myelin lipid layers, Gaussian is preferred for its computational simplicity.

Matrix A and matrix E, coefficient matrices, could be time dependent or independent based on the RF field strength B_1 . As explained in section 2.4.3 and depicted in the modified Bloch equations, line-shape of the pools depends on B_1 which in turn depends on the pulse shape and pulse width. In the case of different pulse shapes like hanning and sinc-gauss, whose B_1 is continuously varying results in a time varying matrices A and E. Since we cannot achieve constant B_1 through out the pulse, a constant B_{1RMS} is considered for simulations. Then we obtain a time independent matrix as all the other parameters are predefined or determined by the system.

The B_1 effect, TR effect and the impact of off-resonance frequency Δ for 7T parameters are studied using simulations. The parameters used for the following studies are listed in Table 3.1.

Table 3.1: Numerical simulations-Dependence of parameters on ihMT for 7T

| parameters | Δ (kHz) | B_{1RMS} (μ T) | TR (ms) | M_0^B (%) |
|-----------------------|----------------|-----------------------|---------|-------------|
| Δ dependence | 4-14 | 7.4 | 100 | 13.87 |
| B_{1RMS} dependence | 10 | 3-7.4 | 100 | 13.87 |
| TR dependence | 10 | 7.4 | 10-300 | 13.87 |

3.1.1 Steady state solution for Matrix differential equation

The general solution for matrix differential equation is used to solve the modified Bloch equations as shown in equation 3.1. The matrix equations for single and dual RF, assumed steady state by applying a constant B_{1RMS} are modelled for repetitive period(TR).

$$M(t + TR) = S \cdot B + (S - I) \cdot A^{-1} \cdot B \quad (3.1)$$

Where $S = e^{A \cdot t}$. By solving the single and dual equations, we get M_Z^S with dipolar component and M_Z^D without dipolar component.

However, there were few challenges in using this technique. Solving matrix exponential $e^{A \cdot TR}$ play an important role in solution of the steady-state equations. Determination of Matrix S for every iteration of TR is computationally expensive and is not practical for larger values of TR. So, a simpler solution not involving computation of matrix exponential is preferred.

3.1.2 Euler’s method

There are many techniques available to solve the differential equations, some of the simpler solutions include ODE solvers. Literature indicated that ODE45 was one of the majorly used techniques in solving modified Bloch equations of ihMT. However, we

choose to work with Euler’s method which is the straightforward way of solving ODEs. The numerical solutions for Euler’s differential equations are given in equation 3.2.

$$y_{n+1} = y_n + h * f(y, t) \quad (3.2)$$

Where y_{n+1} is $M(t+TR)$, current value of longitudinal magnetization of pools which is to be calculated, y_n is $M(t)$, preceding value of longitudinal magnetization of pools and $f(y,t)$ represents $M_Z^A(t)$, $M_Z^B(t)$ (and $\beta(t)$) in function of various parameters. $h = t_{n+1}-t_n$, is the step size or the time difference between consecutive steps.

To estimate the longitudinal magnetization of the pools at the end of repetition time(TR), Euler’s forward method is applied for single and dual RF equations. To minimize the error and obtain better accuracy, step size is to be very small. In this study, $h=0.001$ is considered [36].

Calculating ihMTR

For calculating ihMTR, we require final longitudinal magnetization of pool A when single RF pulse is applied(M_S), when dual RF pulse is applied(M_D) and without any RF pulses for longitudinal magnetization at equilibrium(M_0). ihMTR calculation is given in equation 3.3.

$$ihMTR = \frac{M_{Z(S)}^A - M_{Z(D)}^A}{M_0} \quad (3.3)$$

All the final calculations for ihMTR are based on the longitudinal magnetization/spin population of pool A since only pool A is MR visible.

3.2 Experimental studies: MRI scan protocol for phantom and in-vivo imaging

The phantom and in-vivo experiments were conducted on 3T clinical scanner(Philips Ingenia, 3T, Best, The Netherlands) and 7T scanner(Philips Achieva, 7T, Cleveland, OH). The ihMT preparation sequence, acquisition protocol and post-processing of phantom and in-vivo data are discussed in this section.

3.2.1 ihMT preparation pulse sequence

A pulsed ihMT preparation sequence implementation is showed in Figure 3.1. N_P pulses separated by an interval(Δt) of 0.45 ms are given prior to acquisition. In between the pulses, a gradient of duration 0.3 ms and strength 10 are given to increase the saturation efficiency.

For EPI acquisition, 6 shaped RF pulses are given with flip angle 90° for each Relaxation time(TR). For TFE, N_P ranging 24 to 300 pulses are used for preparation, depending on B_0 and B_1 values.

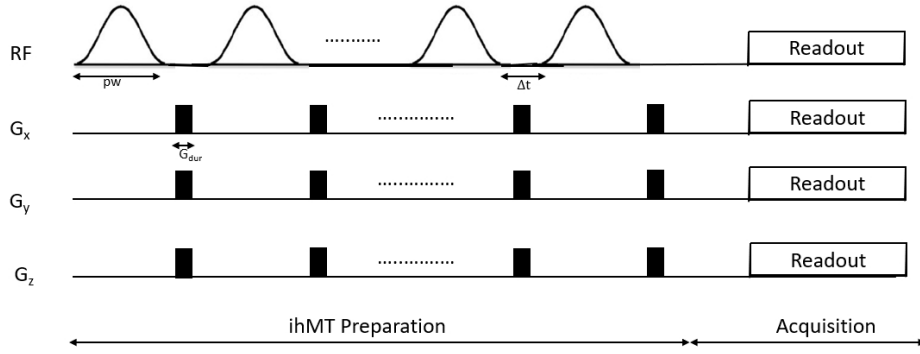


Figure 3.1: Pulsed ihMT acquisition

RF pulse properties such as peak value of B_1 /pulse amplitude and pulse width(pw) are inter-dependent. By varying pulse width, maximum B_1 is set. B_{1RMS} gives effective B_1 of the pulse, depends on the shape, inter-pulse interval and number of pulses.

$$B_{1RMS}^2 = \int^{\tau} B_1^2(t) d\tau \quad (3.4)$$

The formula for calculating B_{1RMS} for hanning pulse is given in equation 3.5[36].

$$B_{1RMS} = \sqrt{\frac{pw}{pw + \Delta t}} \times \sqrt{0.375} \times B_1 \quad (3.5)$$

For ihMT processing, we acquired a set of five images as discussed in section 2.4.4. For Single RF, shaped pulses are applied at either positive or negative off-resonance frequency (Δ). For dual RF pulse generation, pulses with alternating $+\Delta$ and $-\Delta$ frequencies separated with an inter-pulse interval(Δt) are used. For reference image, we need acquisition with no preparation pulse. However acquiring such signal could create complications in timing with respect to acquisitions with preparation pulses. To have comparable timings for each image acquisition, we saturate the sample with 500 KHz frequency.

3.2.2 Data Acquisition

The scan parameters for acquisition were the following: Field of View(FOV) 255 x 255 x 35 mm^3 , voxel size 2.5 x 2.5 x 5 mm^3 , flip angle is set to 7° .

3.2.2.1 Phantom studies

A phantom is prepared by placing 90 ml of hair conditioner in a 100 ml container. The chemical composition of hair conditioner include suspension of fatty acids which have structural similarities to the methyl chains in lipid layers of myelin. The fatty acid structure mimics the residual dipolar coupling and thereby exhibits a strong ihMT effect [32]. Presence of any air bubbles in the phantom could result in susceptibility

artifacts in MR imaging. To avoid that, the container is vacuumed to extract any air bubbles present in the sample. Phantom is placed in the head coil of 3T and 7T scanner with 2 channel transmitter and 32 channel receiver and imaged.

With phantom, five different studies were conducted. 1) Study of impact of fast imaging techniques on ihMTR and scan duration 2) Impact of off-resonance frequency on ihMTR 3) Study of B_1 effect 4) Impact of RF pulse profile on ihMT 5) Impact of number of RF pulses on saturation and ihMTR. The scan parameters used for the each study at 3T and 7T are given in Table 3.2.

For 3T, fast imaging techniques like Turbo Field Echo (TFE), Echo planer Imaging (EPI) are compared along side the conventional MRI acquisition. For EPI, 7 readout-segments are used for image acquisition while for TFE, with factor 20, 30 and 70 indicating the k-space lines acquired are compared for image acquisition. For 7T, EPI 7 and TFE 70 with profile order low-high and linear are tested.

Table 3.2: Phantom studies-ihMT dependence on parameters for 3T and 7T

| Parameters | Acquisition | Δ kHz | B_1/B_{1RMS} μ T | N_P | Pulse shapes |
|---------------------|-------------|--------------|--------------------------------------|------------------|---|
| Fast Acquisition | EPI | 8 | 20 (7T) | 48 | Hanning |
| | TFE | | 18 (3T) | 6 | |
| | No fast | | | | |
| Δ Dependence | TFE | 4-16 | 18, 14, 10(7T) 18, 14(3T) | 100 | Hanning |
| B_1 Dependence | TFE | 10 | 6-20 | 100 | Hanning |
| Pulse Profiles | TFE | 10 | 16 / 5 | 100 | Hanning Hperbolic-secant Sinc-Gauss |
| N_P dependence | TFE | 10 | 19, 16 (7T) 10 (7T) 19, 16, 10 | 50-100 50-200 | Hanning |

The main objective is to optimize the preparation and acquisition parameters to achieve maximum ihMT effect in human brain. For optimizing each parameters, it is to be tested for all the possible values and since we aim to work on more than one main parameters, it is difficult to achieve that with limited subjects for in-vivo imaging. Phantom mimics myelin condition in the human brain and based on phantom results, a minimized set of values for each parameters are tested in in-vivo imaging.

3.2.2.2 In-vivo imaging

For in-vivo imaging, 6 volunteers were scanned on a 7T scanner and 5 volunteers were scanned on 3T scanner. Since this study is focused on feasibility, only a small portion of brain is imaged. During the scan planning, a part of the brain is selected as shown in Figure 3.1. Approximately, same section of brain is selected for all the volunteers. FOV 246x246x35 and voxel size 2.5x2.5x5 mm^3 is maintained during all the in-vivo

experiments to achieve an impartial comparison of 3T and 7T. We used TFE readout with factor 70 for image acquisition.

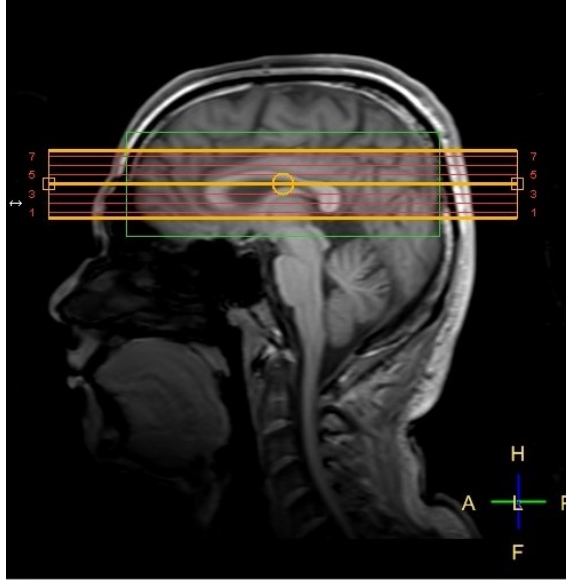


Figure 3.2: Scan planning for in-vivo imaging

At 7T, all the locations of the image do not reach the desired B_1 due to inhomogeneities. In some regions, it reached 90% of maximum B_1 whereas some regions of the brain achieved only 60% of B_1 . We tried to improve the B_1 by increasing the power supplied to RF drive scales. However, there are limitations to maximum allowable power to RF drive scales(4000 W per transmit channel for 7T).

Impact of Δ , B_1 , pulse shapes and N_P are examined on human subjects. The protocol used for study of each parameter is presented in Table 3.3.

Table 3.3: In-vivo imaging- ihMT dependence on parameters for 3T and 7T

| Parameters | Acquisition | Δ kHz | B_1/B_{1RMS} μT | N_P | Pulse shapes |
|---------------------|-------------|--------------|------------------------------|----------------------------|--|
| Δ Dependence | TFE | 4-14 | 18 | 100 | Hanning |
| B_1 Dependence | TFE | 9 | 10-20 | 100 | Hanning Hyperbolic-secant |
| Pulse Profiles | TFE | 7 | 16 / 5 | 100 | Hanning, Hyperbolic-secant, Sinc-Gauss |
| N_P dependence | TFE | 9 | 19 | 50-100 (7T) 50-300 (3T) | Hanning Hyperbolic-secant |

3.2.3 Selection of ROI

All the post processing of phantom and in-vivo data is done in MATLAB (R2019a). Image acquisition resulted in 2D images of 7 slices for phantom and human brain.

For phantom, assuming the fatty acids are uniformly distributed in the sample, ROI is selected on the middle slice. The same slice and ROI are used for the rest of the experiments in optimizing a parameter.

In brain, almost 14% of white matter is myelin whereas in grey matter, it is less than 2%. For better quantitative assessment of myelin, the middle slice is selected and ROI is drawn in the white matter[1].

In Figure 3.3, it can be observed that an interactive polygon is drawn in white matter. The average of the myelin content from that region is obtained as ihMTR. Same ROI is used for rest of experiments from the same subject while optimizing a parameter.

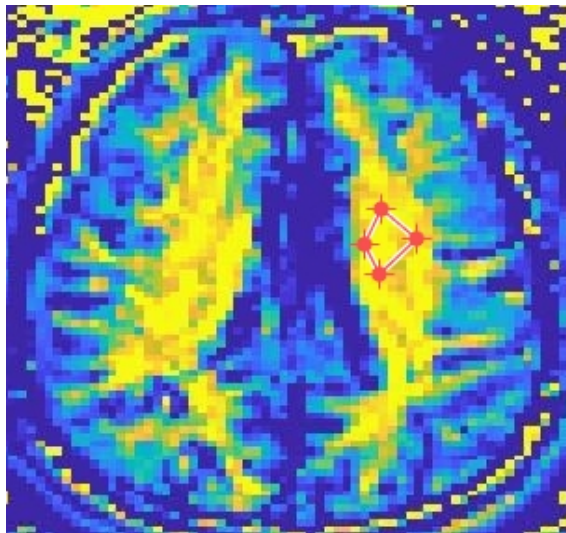


Figure 3.3: Selecting ROI in white matter of human brain

Results

4.1 Simulation Results

The modified Bloch simulations were used in studying impact of various scan parameters on ihMTR at 7T. The influence of B_{1RMS} on the ihMTR is shown in figure 4.1a. The ihMTR increases with an increase in B_{1RMS} as power of RF pulses is very essential for saturation. With low B_{1RMS} , only a small portion of macro-molecular is saturated. With increasing B_{1RMS} , the saturation power increases, improving ihMTR. B_{1RMS} ranging from 3 to 7.4 μT are tested to align with maximum achievable B_{1RMS} at the 7T scanner.

From figure 4.1b, it can be concluded that from 0 to 75 ms ihMTR increases with increase in TR. At approximately 75 ms, we can observe the maximum ihMTR indicating maximum saturation is achieved. After 75 ms, the ihMTR drops in its value with increasing TR. However it is not possible to attain such low TR in the scanner due to system restrictions.

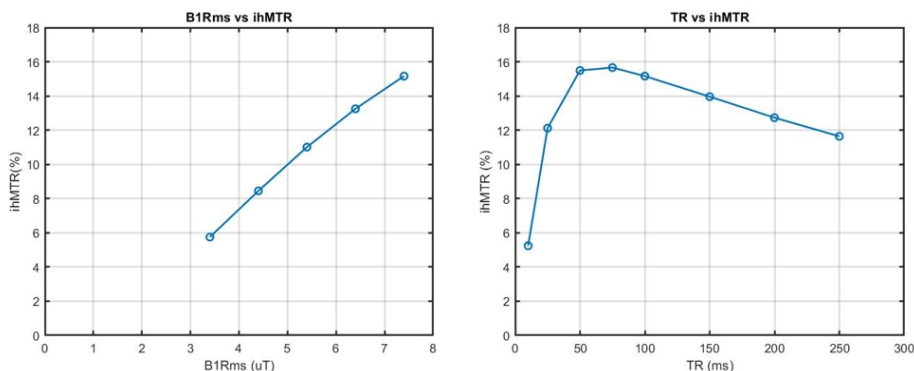


Figure 4.1: a. B_{1RMS} vs ihMTR b. TR vs ihMTR

Based on the literature study on ihMT at 1.5T and 3T, the off-resonance frequency is varied from 2-16 KHz.

Even though we observed the maximum signal at 10 KHz from figure 4.2. One of the major impact of this result is the absorption line-shape of macro-molecular pool. Since gaussian gives the approximation of spin interactions in motion restricted systems in non-biological structures, it might not give very accurate depiction of myelin. Because of mentioned reason, $\Delta = 10\text{KHz}$ might not be optimized value for in-vivo imaging.

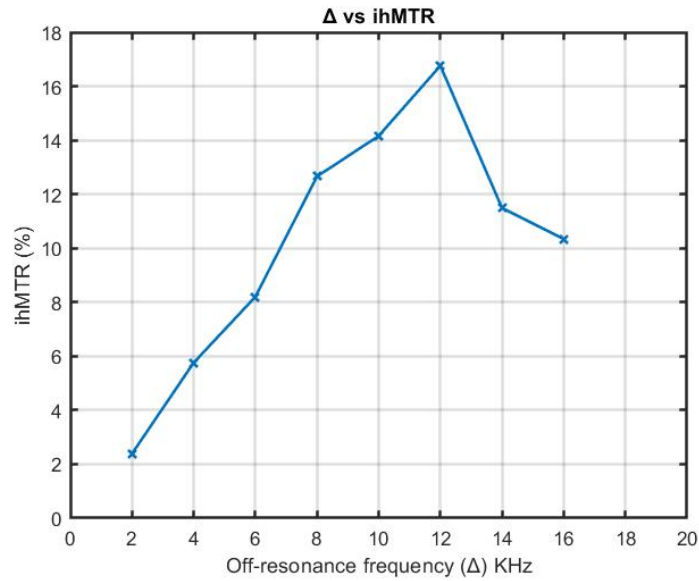


Figure 4.2: Off-resonance frequencies vs ihMTR for 7T parameters using Euler's method

4.2 Experimental results: Phantom and in-vivo imaging

In this section, the effect of off-resonance frequency Δ , B_1 , Pulse shapes and

4.2.1 Acquisition modes

In this section, results of acquisition techniques implemented for phantom experiments at 3T and 7T are discussed. Acquisition modes play an important role in indirect measure of myelin using ihMT. Fast imaging techniques like EPI and TFE decrease the scan time greatly and also contribute to image quality due to reduced subject motion. Few of the acquisition modes were experimented at 3T and 7T. The results obtained are shown in Figure 4.3. Comparison of acquisition methods for 3T is done based on

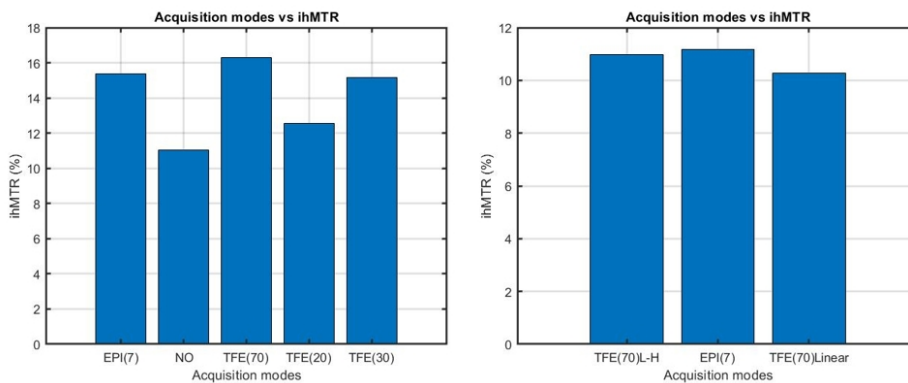


Figure 4.3: a. Acquisition modes vs ihMTR at 3T b. Acquisition modes vs ihMTR at 7T

the scan duration and ihMTR.

Table 4.1: Comparison of acquisition techniques for phantom at 3T

| Image acquisition | Scan duration min:sec | ihMTR % |
|-----------------------------|--------------------------|---------|
| Conventional MR acquisition | 02:18 | 11.04 |
| EPI with 7 segments | 00:49 | 15.39 |
| TFE factor 70 | 00:30 | 16.28 |
| TFE factor 30 | 00:25 | 15.18 |
| TFE factor 20 | 01:14 | 12.55 |

In Figure 4.3, TFE with factor 70($TR/TE = 3/1.71$ ms) outperforms all the others followed by EPI factor 7($TR/TE=100/3.1$ ms) which provides the second highest ihMT ratio. At 7T, experiments are conducted with TFE and EPI acquisition. Total scan time of TFE at 7T is 55.5 seconds while EPI is 1 minute 36 seconds.

For both 7T and 3T, TFE and EPI have comparable ihMTR but images with EPI are geometrically distorted. Phantom is contained in a cylindrical container with circular opening. With EPI, the distortion in the shape of the container thereby in the phantom is clearly seen in Figure 4.4. While, with TFE, this artifact is clearly eliminated and delivered promising results in the image acquisition. For further experiments, to optimize the preparation sequence, TFE with a factor 70 and profile order low-high is applied for acquisition.

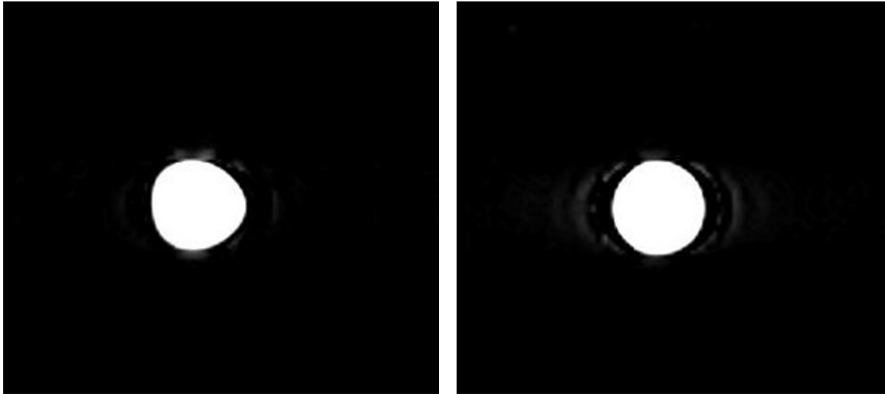


Figure 4.4: A. Phantom scan of one of the 7 slices using EPI for acquisition with geometrical distortion B. Phantom scan using TFE acquisition.

4.2.2 Influence of off-resonance frequency (Δ)

The off-resonance frequency at which RF pulses are to be applied is very crucial for targeting the macro-molecular pool. Specific ranges of off-resonance frequencies will affect a particular component of the macro-molecular pool.

Phantom results

Based on the results from literature study, to optimize off-resonance frequency at 7T, we designed experiments with frequencies ranging from 4 to 16 kHz with step size of 2 kHz and 1 kHz between 6-10 kHz.

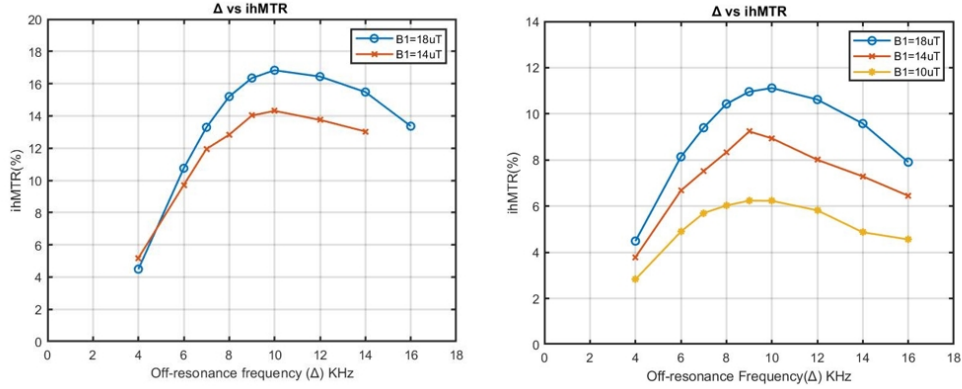


Figure 4.5: Comparison of off-resonance frequencies vs ihMTR % for different B_1 s at 3T and 7T from phantom

Frequencies 9-10 kHz away from the water pool have significant influence on ihMTR with nearly 11.6%. Δ vs ihMTR is checked at two different B_1 s for 3T for $B_1 = 14 \mu\text{T}$ and $B_1 = 18 \mu\text{T}$. Both of them showed similar pattern with maximum contrast at 10 KHz. For 7T, 3 different B_1 s are considered with field strengths $10 \mu\text{T}$, $14 \mu\text{T}$ and $18 \mu\text{T}$. When experimented with $14 \mu\text{T}$ and $18 \mu\text{T}$, the maximum is obtained at 9 kHz and 10 kHz respectively. An additional B_1 of $10 \mu\text{T}$ is tested to investigate any possibility of shift in targeted off-resonance frequency with change in B_1 . We observed similar results as 3T with the maximum ihMTR concentrated in the range of 9-10 kHz away from water frequency. Off-resonance frequencies (Δ) against ihMTR results for different B_1 s at 3T and 7T are shown in Figure 4.5.

For comparing 3T and 7T impact on the ihMTR, B_1 is set to $18 \mu\text{T}$. At 3T, ihMTR is around 17% while at 7T, it is 11%.

In-vivo results

Based on the phantom results, the test set of off-resonance frequency(Δ) for in-vivo imaging is reduced to 4-14 kHz. From the Figure 4.7, it can be observed the maximum ihMT signal is observed at 8 kHz for 3T and 9 kHz for 7T . As the experiments are dependent on the interplay of complex parameter, there could be variations in optimizing the imaging parameters of 3T and 7T.

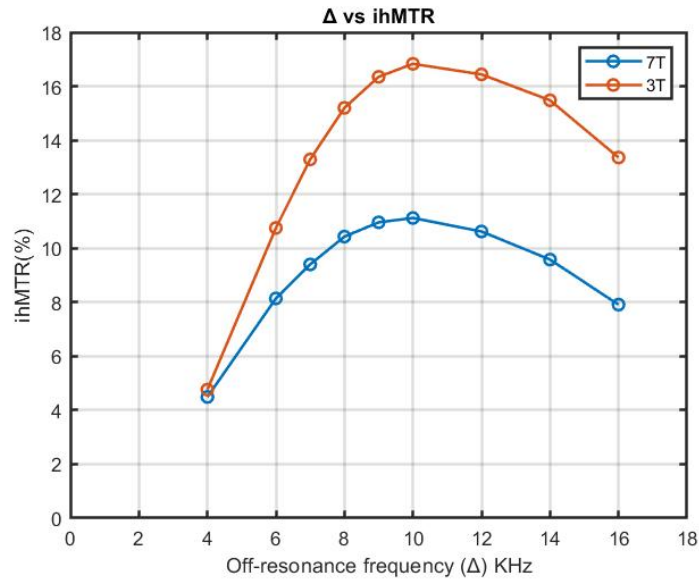


Figure 4.6: Comparison of off-resonance frequencies vs ihMTR % for 3T and 7T from Phantom

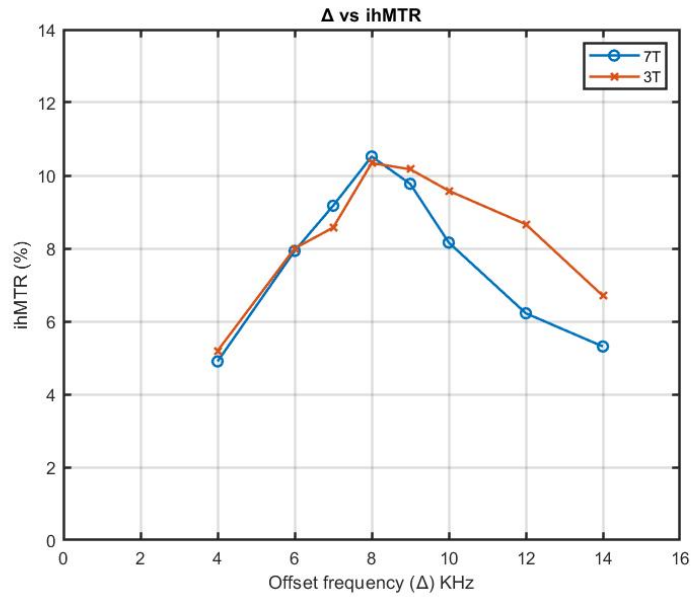


Figure 4.7: Off-set frequency Δ vs ihMTR 3T and 7T from in-vivo human brain

4.2.3 Influence of Pulse shape

For preparation pulses, hanning, Hyperbolic-secant and Sinc-gauss are reviewed. B_1 and pulse width are interdependent. With various pulses, we can achieve required B_1 at different pulse widths. Due to the shape and property differences in pulses, fixing the maximum B_1 strength will not provide a true comparison. For achieving a true comparison, we fixed the B_{1RMS} thereby restricting the energy consumption of each

pulse. In this study, we set the B_{1RMS} to $5.02 \mu\text{T}$ with corresponding maximum B_1 of $16 \mu\text{T}$.

Phantom Results

From the Figure 4.8, we derived two inferences, 3T performance overshadowed 7T and Sinc-gauss has highest contrast at both magnetic field strengths. At 3T, Sinc-gauss achieved 14% and at 7T, 9.5%. Despite its better performance compared to other two pulse shapes, Sinc-gauss is not considered for further research. Due to the system restrictions, the maximum achievable B_{1RMS} for Sinc-gauss is $5.02\mu\text{T}$ which is quite less than threshold RF field strength. On the other hand, hanning can achieve B_{1RMS} up to $7.5 \mu\text{T}$ making it a better option at higher B_1 to obtain maximum ihMTR.

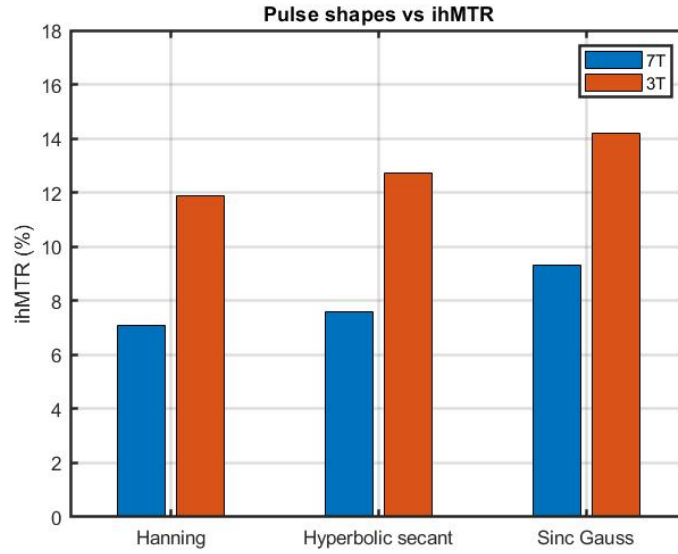


Figure 4.8: Pulse shapes vs ihMTR at 3T and 7T from phantom

By fixing B_{1RMS} of the pulses, we are restricting the maximum achievable B_1 to $16\mu\text{T}$ which is less compared to achievable B_1 at 7T and 3T. With increase the maximum allowable B_1 above $16 \mu\text{T}$, hanning has higher B_{1RMS} compared to other pulse shapes. At $18 \mu\text{T}$, hanning pulse has $B_{1RMS} = 6.96\mu\text{T}$ while hyperbolic-secant has only $5.77 \mu\text{T}$ and Sinc-Gauss $5.30\mu\text{T}$. With $B_{1RMS} = 5\mu\text{T}$, the maximum achieved ihMTR is approximately 8% using Hyperbolic-secant. The pulse properties such as N_P , B_1 (peak power of the pulse) and pulse properties are interrelated.

In-vivo results

At high static field strength (B_0), there is severe inhomogeneity in RF field (B_1). This results in variation of achieved pulse angles at different locations in the brain. This

further results in deviation of SNR and contrast in the images based on the pulse sequence. Due to their insensitivity to RF inhomogeneity, adiabatic pulses perform better than usual RF pulses. Hyperbolic-secant is considered a adiabatic pulse which explains its better performance than other pulse shapes at 7T.

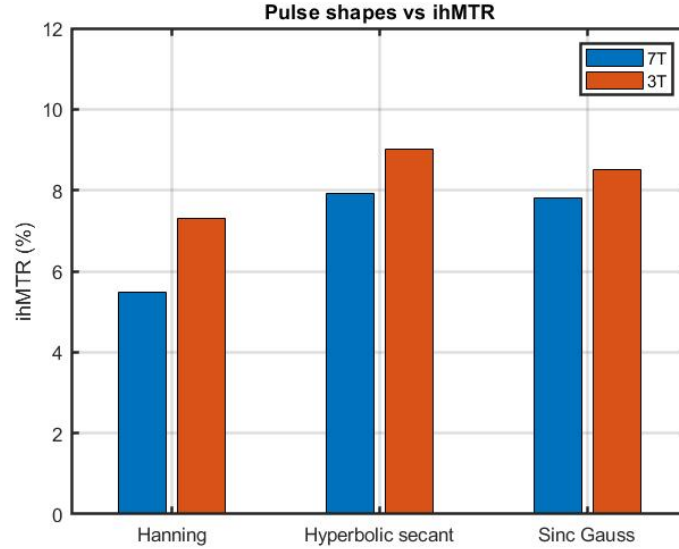


Figure 4.9: Pulse-shapes vs ihMTR at 3T and 7T from in-vivo human brain

4.2.4 Influence of RF field strength (B_1)

At lower RF field strength (B_1), there is not enough power to saturate sufficient protons from pool to provide contrast.

Phantom Results

Maximum B_1 amplitude of 6-20 μT against ihMTR is plotted for 3T and 7T. From the Figure 4.10, it is clearly observed that at 3T, the maximum saturation is obtained at B_1 of strength 19 μT . Above that strength, the ihMTR reduces with an increase in field strength. At 7T, there is an increase in ihMTR with B_1 in almost linear manner but the aggregate improvement is quite less above the field strength of 18 μT . We can expect to reach the maximum threshold around 21 μT but could not confirm due to restrictions on maximum allowable B_1 of 20 μT on scanners. At 3T, with maximum saturation, we get nearly 18% and at 7T close to 12%.

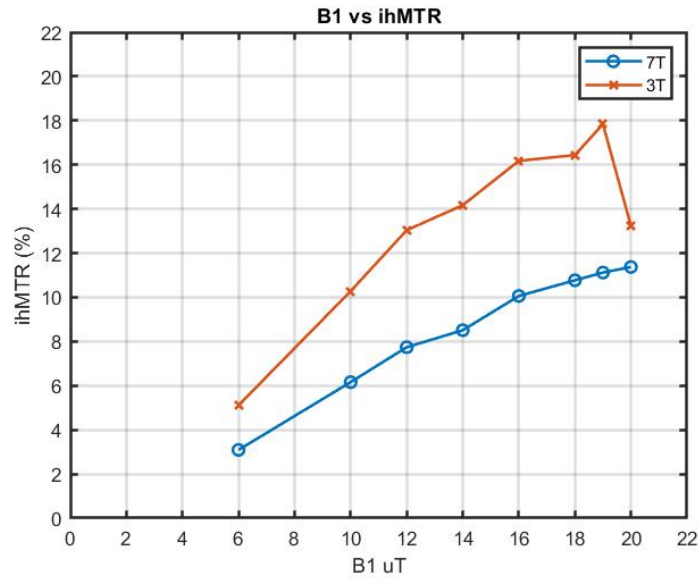


Figure 4.10: RF strength B_1 vs ihMTR for 3T and 7T from phantom

In-vivo results

From the Figure 4.11a, it can be observed that hanning, which is not insensitive to B_1 inhomogeneties suffers greatly at ultra-high fields and performs consistently better at 3T which experiences less B_1 issues.

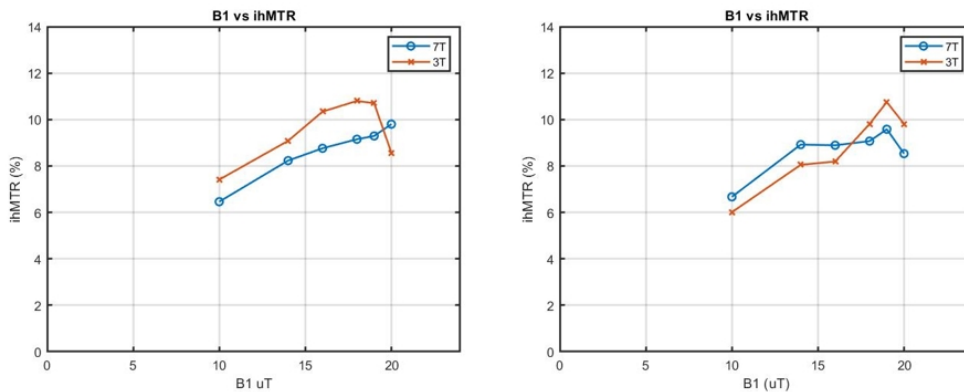


Figure 4.11: a. B_1 vs ihMTR at 3T and 7T when preparation sequence is composed of 100 hanning pulses from in-vivo human brain. b. B_1 vs ihMTR at 3T and 7T when Hyperbolic-secant pulses are used for preparation from in-vivo human brain.

With 3T, we achieve the maximum saturation around 19 μT for both hanning and hyperbolic-secant pulses. However for 7T, with hanning pulse we did not achieve saturation and higher RF field strengths are not tested due to restrictions on maximum allowable B_1 . AT 7T, due to B_1 inhomogeneity, the desired B_1 is not achieved and it can have large difference between peak B_1 and B_1 values attained at different locations

in the image. Based on ROI selection, there could be significant variation in ihMTR.

With hyperbolic-secant, at lower RF field strength 7T performs better than 3T because of resolved inhomogeneity issue. From figure 4.11b, it can be said that until $16 \mu\text{T}$ hyperbolic-secant performs better than hanning at 7T. The drop in increase of B_{1RMS} do not work well for hyperbolic-secant against inhomogeneties at 7T.

4.2.5 Influence of number of pulses (N_p)

Number of pulses in the preparation sequence also contribute to the amount of saturation. Using few pulses can result in inadequate saturation affecting the contrast. But at higher B_1 , due to SAR restrictions, we cannot use more than a certain number of pulses, however at lower B_1 , we can feed up to approximately 200 pulses for the preparation sequence.

Phantom Results

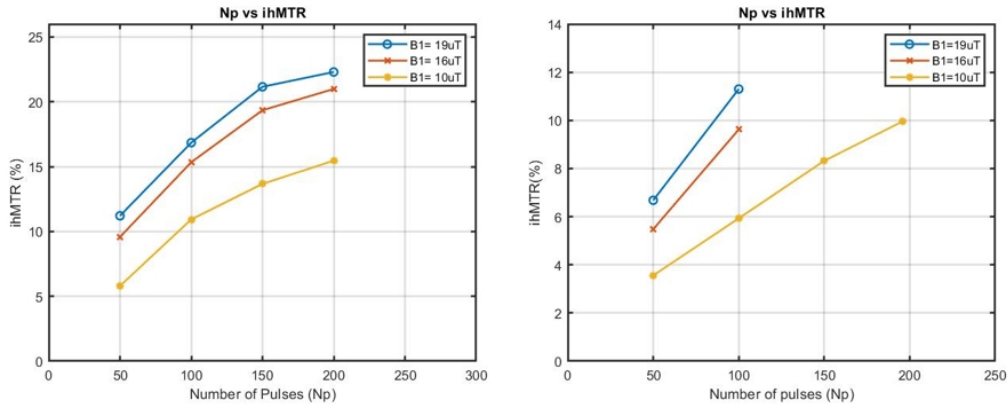


Figure 4.12: a. Number of Pulses vs ihMTR at 3T for different B_1 strengths for Phantom b. Number of Pulses vs ihMTR at 7T for different B_1 strengths from phantom

At 3T, we can feed 200 pulses in preparation sequence at all three tested B_1 s of $10 \mu\text{T}$, $16 \mu\text{T}$ and $19 \mu\text{T}$. From the Figure 4.12, the deductions are quite clear that with increase in number of pulses, there is improvement in contrast and results are consistent with different B_1 , showcasing the B_1 effect as well. At 7T, we can reach only a maximum of 100 pulses for $B_1 = 16 \mu\text{T}$ and $19 \mu\text{T}$ due to strict SAR restrictions. From the figure, we can see that sequence with $N_p = 100$ at $B_1 = 18\mu\text{T}$ has higher ihMT than sequence with $N_p = 200$ at $B_1 = 10\mu\text{T}$. This solidifies the extent of B_1 impact on ihMTR. A comparison of 3T and 7T for $B_1 = 19 \mu\text{T}$ is provided in the Figure 4.13.

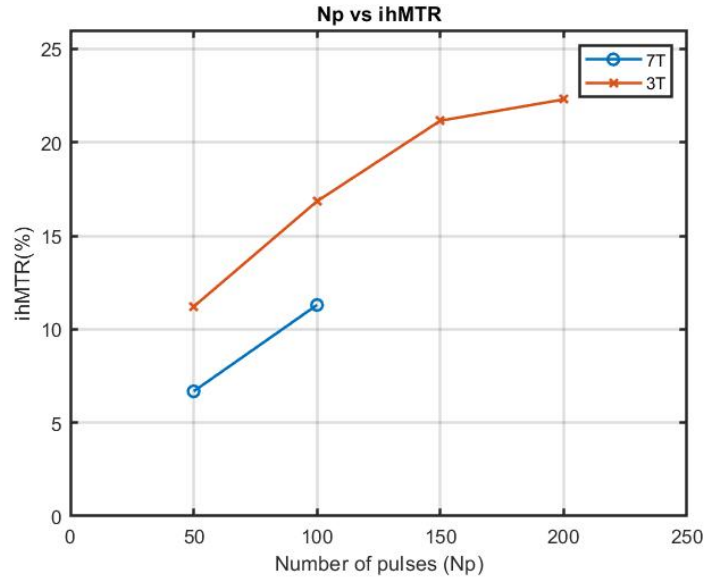


Figure 4.13: Number of Pulses vs ihMTR at 3T and 7T from phantom

In-vivo results

The RF frequency is set as 8KHz based on optimized parametric value and B_1 is $18\mu\text{T}$ for both 3T and 7T experiments on N_P . Based on the phantom results, it is established that increasing number of pulses improves the amount of saturation. Also in in-vivo results, with increase in number of pulses, ihMT improved with increase in N_P till 200 pulses. For hyperbolic-secant, it is not checked at 200 pulses due to time

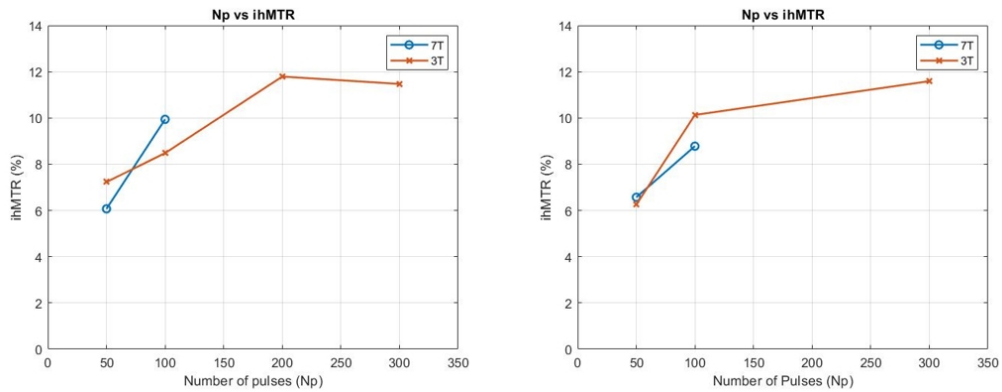


Figure 4.14: a. N_P vs ihMTR at 3T and 7T when hanning pulse is used for in-vivo human brain. b. N_P vs ihMTR at 3T and 7T when hyperbolic-secant is used from in-vivo human brain.

limitation but similar trend can be expected. With approximately 200 pulses in the preparation sequence, the maximum saturation of macro-molecules is achieved thereby attaining maximum ihMTR. Any further increase in N_P , we observe no improvement in saturation and ihMT.

4.3 Optimized protocol for phantom and in-vivo imaging

Based on the results of the experiments, optimized scan parameters for achieving highest ihMTR for phantom and in-vivo imaging for 3T and 7T are presented in Table 4.2.

Table 4.2: Optimized parameters for Phantom and in-vivo imaging at $B_0 = 3\text{T}$ and 7T

| Parameters | Δ kHz | B_1 μT | Pulse shapes | N_P | ihMTR (%) |
|-------------------|--------------|---------------------|-------------------|-------|----------------|
| Phantom 3T | 10 | 19 | Hanning | 200 | 23% \pm 0.9% |
| Phantom 7T | 10 | 20 | Hanning | 100 | 11% \pm 0.5% |
| In-vivo 3T | 8 | 18-19 | Hanning | 200 | 12% \pm 0.8% |
| | | 19 | Hyperbolic-secant | 300 | |
| In-vivo 7T | 8 | 20 | Hanning | 100 | 10% \pm 1% |

The final in-vivo brain images at 3T and 7T using their respective optimized protocols are shown in Figure 4.15. From the Figure 4.15, it can be clearly observed that image of brain at 3T show better contrast compared to 7T. This is because of the number of pulses in its preparation sequence, 3T has 200 hanning pulses resulting 326.29 ms saturation duration while 7T has only 162.99 ms of saturation.

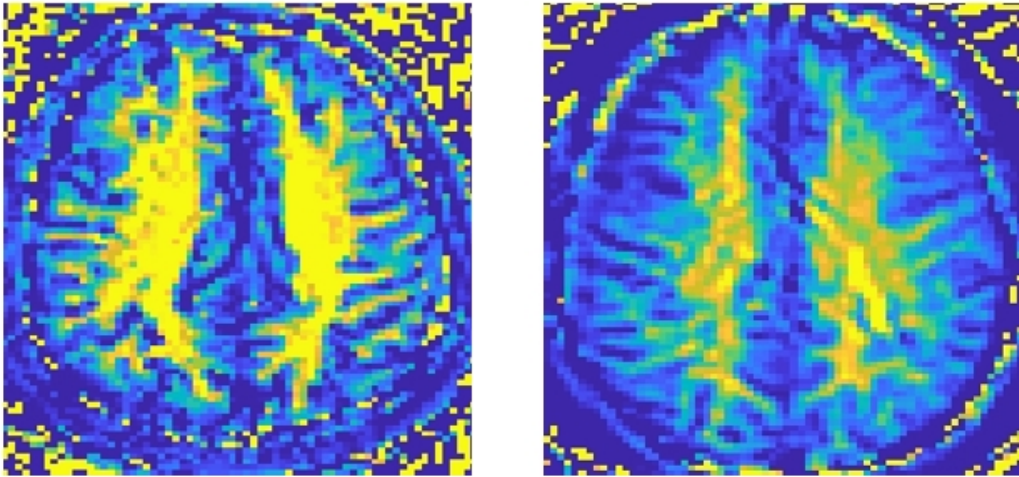


Figure 4.15: a. In-vivo image with optimized protocol at 3T displaying maximum ihMT effect. b. In-vivo image with optimized protocol at 7T

The ihMT effect in 7T images is restricted by the number of pulses allowable at higher B_1 (More than 16 μT).

Discussion

This work demonstrated the implementation of ihMT at $B_0 = 3\text{T}$ and 7T . All the experiments are conducted on healthy volunteers. The methods provided an outline of numerical simulations of modified Bloch equations and a MRI protocol used for phantom and in-vivo imaging at 3T and 7T .

Simulations

The numerical simulations provided the basic framework of ihMT preparation. The simulations were done for 7T parameters. The simulation results from Figure 4.1b show the impact of B_{1RMS} on ihMT, inferring the increase of ihMT effect with increase in B_{1RMS} . Since RF field strength decides the amount of saturation exchange between the pools, any values lower than $3 \mu\text{T}$ will not give a true impression of myelin content. Similar trends of B_{1RMS} is observed in the previous studies on ihMT with 1.5 T parameters, ihMTR increased with an increase in B_{1RMS} from 2 to $6 \mu\text{T}$ with maximum of 14% [26].

With 7T numerical simulations, we observed optimum TR at 75 ms . Based on the test set of numerical simulations, TR is tested at 7T and 3T for phantom. For TFE acquisition, TR is fixed, so TR impact is studied using EPI acquisition and comparison of 3T and 7T is presented in appendix Figure. A.3. With an increase in TR, ihMTR decreased at both magnetic field strengths. We could not test for TR lower than 50 ms for 3T and 150 ms for 7T due to system restrictions which are incidentally best TR for the respective magnetic field strengths.

As explained in section 2.2, macro-molecular spectrum is quite broad. Each component of the pool is sensitive to a specific range of off-resonance frequency. For better understanding of the myelin content, it is important to identify the target Δ range. From the Figure. 4.2, a maximum of 17% ihMTR is observed at 10 kHz . However, the distinguishable bell-curve of off-resonance frequency Δ vs ihMTR is not achieved which was expected based on literature study. This could be because of the absorption line-shape of the macro-molecular used in the simulations. Since myelin sheath is wound around axons, the signal might come from 0 to 90° . Super-lorentzian would be a better choice as it integrates the signal from all the angles and known to be an accurate depiction of line-shapes in biological systems. Also, initial β is extremely important when single off-resonance frequency is applied. Even slightest variation in the value had an scaling impact on the ihMTR. However, even with gaussian line-shape, maximum ihMT is observed in the expected $8\text{-}10 \text{ kHz}$ range. Numerical simulations dealt with only the ihMT preparation stage. The results from the numerical simulations were used in deciding the test parameters for phantom. From the simulation results of [26] for 1.5

T parameters, a maximum of 17% is noted in 7-9 kHz range with B_{1RMS} of 5.5 μ T.

Comparison of phantom and in-vivo results

The phantom studies provided insight on impact of the parameters on ihMTR. The optimized protocol for phantom at 3T and 7T showed approximately 6% (17%-11%). However, we did not observe much difference in case in-vivo imaging, with both attaining a maximum of 12% for 3T and 10% for 7T (refer figure 4.7). The phantom results provide the impact of various parameters and also form basis for optimizing the protocol for the in-vivo imaging. The results of phantom and in-vivo are expected to slightly differ, as the dipolar relaxation times are different in brain tissue when compared to the phantom.

In phantom, the sample is concentrated and assumed to be uniformly distributed, however, the same cannot be said for the myelin concentration and distribution in human brain. As discussed in section 2.1, myelin concentration is higher in white matter which is located in inner layers of brain connected by grey tissue on the outer layers. The ratio of myelin in white matter to grey matter is known to be approximately 1 to 3 hence the simulation parameters for 7T are taken based on white matter in human brain and also the ROI selected in WM for acquired in-vivo images.

Despite the increase in saturation duration to maximum of 514.36 ms, we attain a maximum of 12% at 3T which emphasizes the impact of macro-molecular pool fraction in brain on ihMT.

Fast imaging techniques

In literature, many studies used Gradient Echo imaging and EPI readouts for image acquisition [32]. In this study, TFE readout is implemented because of reduction of scan duration and to avoid geometrically distorted images.

The preparation sequence is composed of minimum N_P of 48 to maximum 300 pulses based on B_0 and B_1 values. In phantom study at 3T, we achieved almost 22% when 200 pulses are used in preparation of ihMT. With total 50 pulses, ihMT saturation duration was only 85.71 ms and with 200 pulses, saturation duration is 342.15 ms. With increase in ihMT saturation duration, larger fraction of macro-molecular pool is saturated resulting in higher ihMTR. Using TFE, we can image the whole brain in 5 minutes which is very useful in clinical imaging.

Impact of saturation parameters on ihMT

One of the key deductions from the experimental data is the impact of off-resonance frequency (Δ) on ihMT. From phantom results Figure 4.5, 4.6 the prominent bell-

shaped curve show that the off-resonance frequencies ranging from 9-10 kHz achieve best ihMTR. Although, the optimal off-resonance frequency for in-vivo imaging is around 8-9 kHz for both 3T and 7T. Our results aligned with the results from literature based on in-vivo imaging at 3T, ex-vivo samples, phantom experiments and animal studies where the maximum range is observed 7-9 kHz range when tested in 2-16 kHz range [7, 26, 32, 33]. For in-vivo studies conducted at 1.5 T [26], a maximum of 13-15% ihMTR is recorded which aligned with our in-vivo studies at 7T.

RF pulse properties and B_1 are strongly inter-dependent. Lower the pulse width, higher the peak amplitude of B_1 . By varying the pulse width, B_1 can be set given the maximum allowable value. From Figure. 4.10, 4.11, we can observe that, with increase in B_1 , there is increase in ihMTR. Higher B_1 is associated with higher B_{1RMS} and this also explains reduced increase in ihMTR % at higher B_1 s due to minimal increase in RMS values. The experimental data of in-vivo studies at 1.5 T [26] has showed similar trends of B_{1RMS} with maximum of 12-15% and in mouse brain ihMTR increased with an increase in B_{1RMS} from 2 to 8 μ T maximum of 5% for B_{1RMS} of 8 μ T [31].

Pulse shapes used in the preparation sequence have great impact on amount of saturation. In previous studies, pulse shapes like hanning, gaussian and rectangle are used but with 7T it is important to check if the following pulses are still practical to implement[37]. To our knowledge, there is no study on suitable pulse shapes for ihMT at any field strength. We studied the impact of hanning, hyperbolic-secant and sinc-gauss pulse shapes at 3T and 7T. For phantom experiments, at both B_0 s, sinc-gauss performed best of all three when B_{1RMS} is fixed as 5 μ T with $B_1 = 16\mu$ T. However, due to greater B_{1RMS} , hanning outperforms both of them at higher B_1 .

Number of RF pulses (N_P) is directly proportional to the saturation duration and ihMT. From figure. 4.13, 4.14, we can clearly observe the impact of N_P . Increased saturation duration would ensure larger fraction of pool is saturated. But once we achieve maximum saturation, further increase in N_P do not serve any purpose and ihMT remains same which can be observed in figure. 4.14a.

Drawbacks of the study

A major discrepancy experienced in in-vivo imaging is comparison of 3T and 7T while optimizing each parameter. Since the set of experiments were conducted on different subjects at 7T and 3T, there could be differences in myelin content between the subjects. This could create inconsistencies in quantifying myelin and calculating ihMTR. Sometimes, with human subjects, we experienced some physiological motion in the brain even though there is no movement of the subject. We were not sure how this effected the ihMT effect, however no noticeable difference is observed in ihMTR. Due to strict SAR and system restrictions, we could not verify the optimum B_1 for 7T using hanning pulse.

Conclusion and Future study

6.1 Conclusion

In this study, we investigated the feasibility of ihMT at ultra-high field ($B_0 = 7\text{T}$) and compared the results to 3T clinical scanners. Impact of off-resonance frequency, B_0 , saturation pulse properties on ihMTR are studied. The modified Bloch equations are solved using Euler's forward method and fitted with 7T white matter parameters of human brain. The numerical simulations and results of phantom experiments are used in optimizing the test set for in-vivo imaging.

Based on the phantom and in-vivo results at 7T, we can say that ihMT is feasible at ultra-high fields. The optimized protocol for in-vivo imaging at 7T is 100 hanning pulses of $B_1 = 20\mu\text{T}$ applied 8KHz away from water frequency. With optimized protocol, we achieved a maximum of 10%. For acquisition, TFE is preferred for its minimum scan duration and having no artifacts in images. Even though, we observed a scaling impact on ihMTR values at 7T and 3T, the trend in which the parameters affected ihMTR was the same. This implies that changing the B_0 do not impact the way saturation parameters affect ihMT.

6.2 Future work

The experimental inferences of in-vivo imaging parameters are based on a small data set of volunteers with varying age and gender which affects ihMT. No volunteer in the study showed any signs of MS, however, myelin content could be different between the healthy subjects as well. Although the optimized values are verified with more than one subject, averaging the ihMTR values for larger subject group could solidify our conclusions on optimized protocol.

The modified Bloch equations and literature suggest the importance of T_{1D} . For dual frequency generation, the preparation sequence is composed of RF pulses which are given in an alternating $+\Delta$ and $-\Delta$ fashion with an inter-pulse interval Δt . The study of impact of Δt and T_{1D} filtering on ihMT at 7T is essential if 7T MRI scanners are to be used in clinical imaging.

One of the major problems experienced at 7T is B_1 inhomogeneity. Hyperbolic-secant pulses, due to their adiabatic nature curtail inhomogeneities up to some extent and perform better at lower B_1 . However, after 16 μT hyperbolic-secant has lower B_{1RMS} compared to hanning so at higher B_1 hanning is used.

Future work should be based on resolving the B_1 inhomogeneity issue at 7T. Achieving the desired B_1 value consistently at all locations in the brain would vastly improve ihMTR or proposing a pulse shape with an adiabatic nature and improved maximum achievable B_{1RMS} would improve the ihMT effect. The saturation parameters like off-resonance frequency, RF pulse properties, B_1 and T_{1D} filtering are to be tested on MS patients to see if the parameters follow a different trend in case of demyelination.

Bibliography

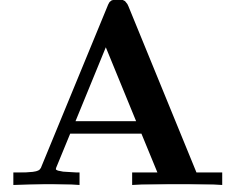
- [1] Y. Min, K. Kristiansen, J. M. Boggs, C. Husted, J. A. Zasadzinski and J. Israelachvili, “Interaction forces and adhesion of supported myelin lipid bilayers modulated by myelin basic protein,” *Proceedings of the National Academy of Sciences*, vol. 106, no. 9, pp. 3154-3159, 2009.
- [2] M. J. Wilhelm, H. H. Ong, S. L. Wehrli, C. Li, P. H. Tsai, D. B. Hackney and F. W. Wehrli, “Direct magnetic resonance detection of myelin and prospects for quantitative imaging of myelin density,” *Proceedings of the National Academy of Sciences*, vol. 109, no. 24, pp. 9605-9610, 2012.
- [3] E. Van Obberghen, S. Mchinda, A. Le Troter, V. H. Prevost, P. Viout, M. Guye, G. Varma, D. C. Alsop, J. P. Ranjeva, J. Pelletier and O. Girard, “Evaluation of the sensitivity of Inhomogeneous Magnetization Transfer (ihMT) MRI for multiple sclerosis,” *American Journal of Neuroradiology*, vol. 39, no. 4, pp. 634-641 2018.
- [4] F. Heath, S. A. Hurley, H. Johansen-Berg and C. Sampaio-Baptista, “Advances in noninvasive myelin imaging,” *Developmental neurobiology*, vol. 78, no. 2, pp. 136-151, 2018.
- [5] Ian D. Duncan, and R. J. M. Franklin, “Myelin Repair and Neuroprotection in Multiple Sclerosis,” *Springer Science and Business Media*, 2012.
- [6] S. D. Wolff, and R. S. Balaban, “Magnetization transfer contrast (MTC) and tissue water proton relaxation in vivo,” *Magnetic resonance in medicine*, vol. 10, no. 1, pp. 135-144, 1989.
- [7] O. M. Girard, V. H. Prevost, G. Varma, P. J. Cozzone, D. C. Alsop and G. Duhamel, “Magnetization transfer from inhomogeneously broadened lines (ihMT): experimental optimization of saturation parameters for human brain imaging at 1.5 Tesla,” *Magnetic resonance in medicine*, vol. 73, no. 6, pp. 2111-2121, 2015.
- [8] B. L. Geeraert, R. M. Lebel, A. C. Mah, S. C. Deoni, D. C. Alsop, G. Varma, and C. Lebel, “A comparison of inhomogeneous magnetization transfer, myelin volume fraction, and diffusion tensor imaging measures in healthy children,” *Neuroimage*, vol. 182, pp. 343-350, 2018.
- [9] S. Love, “Demyelinating diseases,” *Journal of clinical pathology*, vol. 59, no. 11, pp. 1151-1159, 2006.
- [10] G. Varma, O. M. Girard, V. H. Prevost, A. K. Grant, G. Duhamel, and D. C. Alsop, “Interpretation of magnetization transfer from inhomogeneously broadened lines (ihMT) in tissues as a dipolar order effect within motion restricted molecules,” *Journal of Magnetic Resonance*, vol. 260, pp. 67-76, 2015.
- [11] Henkelman, R.M., Stanisz, G.J. and Graham, S.J., “Magnetization transfer in MRI: a review,” *NMR in Biomedicine: An International Journal Devoted to the*

- Development and Application of Magnetic Resonance In Vivo*, vol. 14, no. 2, pp. 57-64, 2001.
- [12] R. S. Balaban, and T. L. Ceckler, "Magnetization transfer contrast in magnetic resonance imaging," *Magnetic resonance quarterly*, vol. 8, no. 2, pp. 116-137, 1992.
- [13] G. B. Pike, "Magnetization transfer imaging of multiple sclerosis," *The Italian Journal of Neurological Sciences*, vol. 18, no. 6, pp. 359-365, 1997.
- [14] R. W. De Boer, "Magnetization transfer contrast Part 1: MR physics," *Medicamundi*, vol. 40, pp. 64-73 1995.
- [15] N. Stikov, "Cross-relaxation imaging: methods, challenges and applications," 2010.
- [16] J. G. Sled, "Modelling and interpretation of magnetization transfer imaging in the brain," *Neuroimage*, vol. 182, pp. 128-135, 2018.
- [17] S. Ropele, and F. Fazekas, "Magnetization transfer MR imaging in multiple sclerosis," *Neuroimaging clinics of North America*, vol. 19, no. 1, pp. 27-36, 2009.
- [18] R. D. Dortch, J. Moore, K. Li, M. Jankiewicz, D. F. Gochberg, J. A. Hirtle, J. C. Gore and S. A. Smith, "Quantitative magnetization transfer imaging of human brain at 7 T," *Neuroimage* vol. 64 pp. 640-649, 2013.
- [19] G. Varma, O. M. Girard, S. Mchinda, V. H. Prevost, A. K. Grant, G. Duhamel, and D. C. Alsop, "Low duty-cycle pulsed irradiation reduces magnetization transfer and increases the inhomogeneous magnetization transfer effect," *Journal of Magnetic Resonance*, vol. 296, pp. 60-71, 2018.
- [20] G. Varma, G. Duhamel, C. de Bazelaire, and D. C. Alsop, "Magnetization transfer from inhomogeneously broadened lines: a potential marker for myelin", *Magnetic resonance in medicine*, 73(2), pp. 614-622, 2015.
- [21] E. Brunner, "Residual dipolar couplings in protein NMR," *Concepts in magnetic resonance*, vol. 13, no. 4, pp. 238-259, 2001.
- [22] S. Aggarwal, Y. Larisa, and S. Mikael, "Central nervous system myelin: structure, synthesis and assembly," *Trends in cell biology*, vol. 21, no. 10, pp. 585-593, 2011.
- [23] O. M. Girard, C. Virginie, V. H. Prevost, R. Benjamin, M. Taso, G. Ribeiro, G. Varma, N. Rangwala, D. C. Alsop, and G. Duhamel, "Magnetization transfer from inhomogeneously broadened lines (ihMT): improved imaging strategy for spinal cord applications," *Magnetic resonance in medicine*, vol. 77, no. 2, pp. 581-591, 2017.
- [24] V. N. Carvalho, A. Hertanu, A. Grélard, S. Mchinda, L. Soustelle, A. Loquet, E. J. Dufourc, G. Varma, D. C. Alsop, P. Thureau and O. M. Girard, "MRI assessment of multiple dipolar relaxation time (T1D) components in biological tissues interpreted with a generalized inhomogeneous magnetization transfer (ihMT) model," *Journal of Magnetic Resonance*, vol. 311, p.106668, 2020.

- [25] S. D. Swanson, D. I Malyarenko., M. L. Fabiilli, R. C. Welsh, J. F. Nielsen and A. Srinivasan, “Molecular, dynamic, and structural origin of inhomogeneous magnetization transfer in lipid membranes,” *Magnetic resonance in medicine*, vol. 77, no. 3, pp. 1318-1328, 2017.
- [26] S. Mchinda, G. Varma, V. H. Prevost., A. Le Troter, S. Rapacchi, M. Guye, J. Pelletier, J. P. Ranjeva, D. C. Alsop, G. Duhamel and O. M. Girard, “Whole brain inhomogeneous magnetization transfer (ihMT) imaging: sensitivity enhancement within a steady-state gradient echo sequence,” *Magnetic resonance in medicine*, vol. 79, no. 5, pp. 2607-2619, 2018.
- [27] Gyromagnetic ratio, https://en.wikipedia.org/wiki/Gyromagnetic_ratio *Wikimedia Foundation*, Feb, 2020.
- [28] C. Morrison, G. Stanisiz and R. M. Henkelman, “Modeling magnetization transfer for biological-like systems using a semi-solid pool with a super-Lorentzian lineshape and dipolar reservoir,” *Journal of Magnetic Resonance*, Series B, vol. 108, no. 2, pp. 103-113, 1995.
- [29] A. P. Manning, K. L. Chang, A. L. MacKay and C. A. Michal, “The physical mechanism of “inhomogeneous” magnetization transfer MRI,” *Journal of Magnetic Resonance*, vol. 274, pp. 125-136, 2017.
- [30] S. Portnoy and G. J. Stanisiz, “Modeling pulsed magnetization transfer,” *Magnetic Resonance in Medicine: An Official Journal of the International Society for Magnetic Resonance in Medicine*, vol. 58, no. 1, pp. 144-155, 2007.
- [31] V. H. Prevost, O. M. Girard, S. Mchinda, G. Varma, D. C. Alsop and G. Duhamel, “Optimization of inhomogeneous magnetization transfer (ihMT) MRI contrast for preclinical studies using dipolar relaxation time (T1D) filtering”, *NMR in Biomedicine*, vol. 30, no. 6, p.e 3706, 2017.
- [32] G. Varma, O. M. Girard, V. H. Prevost, A. K. Grant, G. Duhamel, and D. C. Alsop, “In vivo measurement of a new source of contrast, the dipolar relaxation time, T1D, using a modified inhomogeneous magnetization transfer (ihMT) sequence,” *Magnetic resonance in medicine*, vol. 78, no. 4, pp. 1362-1372, 2017.
- [33] V. H. Prevost, O. M. Girard, G. Varma, D. C. Alsop and G. Duhamel, “Minimizing the effects of magnetization transfer asymmetry on inhomogeneous magnetization transfer (ihMT) at ultra-high magnetic field (11.75 T),” *Magnetic Resonance Materials in Physics, Biology and Medicine*, vol. 29, no. 4, pp. 699-709, 2016.
- [34] K. Setsompop, D. A. Feinberg and J. R. Polimeni, “Rapid brain MRI acquisition techniques at ultra-high fields,” *NMR in Biomedicine*, vol. 29, no. 9, pp. 1198-1221, 2017.
- [35] S. J. Malik, R. P. Teixeira, D. J. West, T. C. Wood and J. V. Hajnal, “Steady-state imaging with inhomogeneous magnetization transfer contrast using multiband radiofrequency pulses,” *Magnetic resonance in medicine*, vol. 83, no. 3, pp. 935-949, 2020.

- [36] A. Iserles, "A first course in the numerical analysis of differential equations," *Cambridge university press*, no. 44, 2009.
- [37] S. J. Graham and R. M. Henkelman, "Understanding pulsed magnetization transfer," *Journal of Magnetic Resonance Imaging*, vol. 7, no. 5, pp. 903-912, 1997.

Appendix



A.1 Phantom results

In this section, we will discuss the effect of various parameters, mainly TR effect in EPI acquisitions. Due to geometrical distortion and scan duration, EPI was not implemented in human brain imaging. However, TFE cannot explain the impact of TR due to fixed value, EPI acquisitions are used to demonstrate the impact of TR on ihMT. Off-resonance frequency and B_1 are also studied.

Off-resonance frequency values from EPI do not deflect much from TFE results with the maximum contrast is obtained from 8-10 KHz. Although ihMTR values are significantly less in 3T and comparable at 7T as depicted in the results of comparison of acquisition modes in figure 4.3. Through out the experiments, total 6 Hanning pulse are used for preparation with $B_1=18\mu\text{T}$ and $\text{TR}=300\text{ms}$.

For B_1 , 3T results resemble the TFE with reduced ihMTR. However at 7T, there is slight deviation. In figure A.2, it can be observed that maximum contrast is obtained at $B_1=18\mu\text{T}$ after which ihMTR is steadily decreasing inferring that maximum saturation is achieved at $18\mu\text{T}$. As we observed the best off-resonance frequency at 8KHz and 9KHz for 7T and 3T respectively, RF pulses are tuned to an off-resonance of 8KHz for optimizing B_1 .

Repetition time(TR) with TFE is fixed so the impact of it on ihMT was not demonstrated. For 3T, TR is tested from 50 to 350ms with step size of 50ms. For 7T, due to system restriction, it is not possible to reach less than 150ms. For the following experiments, Hanning pulses with off-resonance 8KHz and $B_1=18\mu\text{T}$ is fixed.

From the figure A.3, it is deduced that for both 3T and 7T, contrast is best at lower TR. With increasing TR, ihMTR steadily decreased and from $\text{TR}=250\text{ms}$ onward, there is no difference between 3T and 7T. This manifests the strong TR effect in

| Parameter | Acquisition | Δ kHz | B_1 μ T | TR ms | Pulse shapes |
|---------------------|-------------|--------------|---------------|---------------------------|---|
| Δ Dependence | EPI | 2-16 | 18 | 300 | Hanning |
| B_1 Dependence | EPI | 7 | 6-20 | 300 | Hanning |
| Pulse Profiles | EPI | 7 | 18 | 300 | Hanning, Hperbolic-secant, Sinc-Gauss |
| TR dependence | EPI | 7 | 10 | 150-350(7T) 50-350(3T) | Hanning |

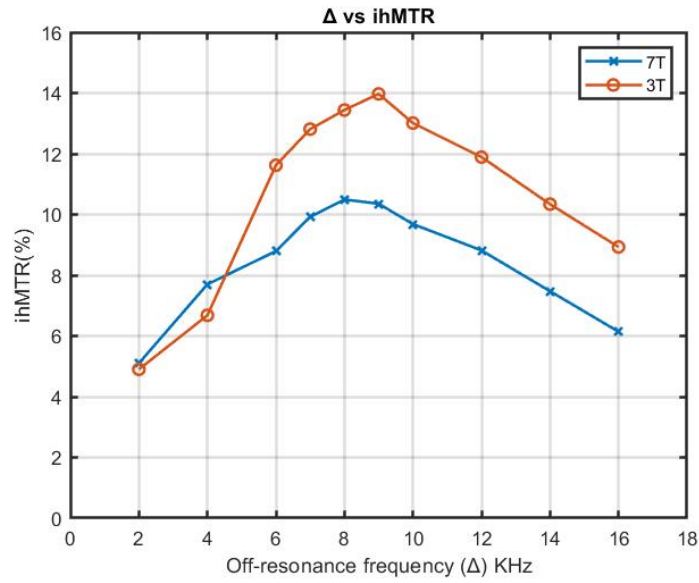


Figure A.1: Off-resonance frequencies vs ihMTR for 3T vs 7T

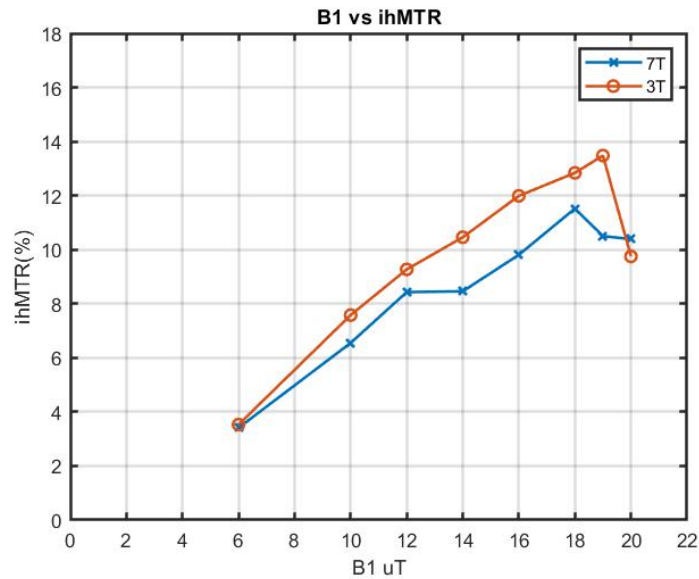


Figure A.2: RF strength B_1 vs ihMTR for 3T vs 7T

ihMT. We observed the same results in numerical simulations.

Pulse shapes are explored with maximum fixed B_1 unlike the TFE experiments, where B_{1RMS} is fixed. From the figure A.4, it shows that due to maximum B_{1RMS} , Hanning performs the best. Due to the shape and pulse width restrictions of system, Sinc-gauss, hyperbolic-secant do not reach the same B_{1RMS} as Hanning.

The optimized parameters for 7T with EPI acquisition are Hanning pulse with 8KHZ

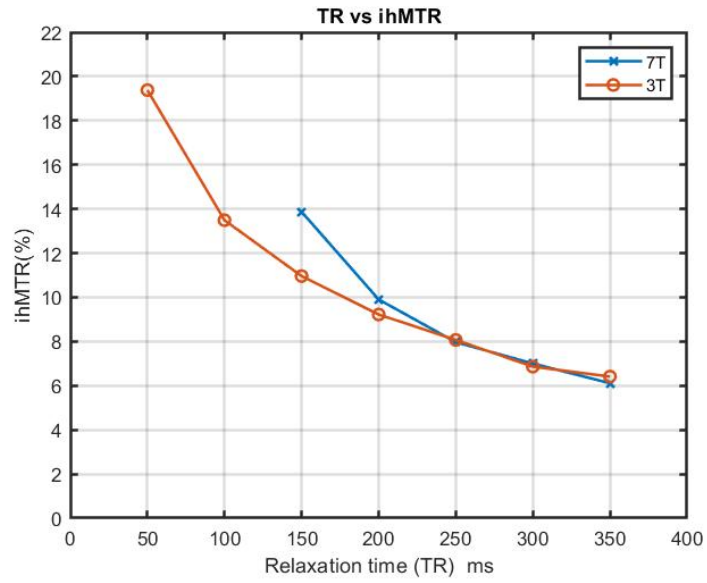


Figure A.3: Repetition time (TR) vs ihMTR for 3T vs 7T

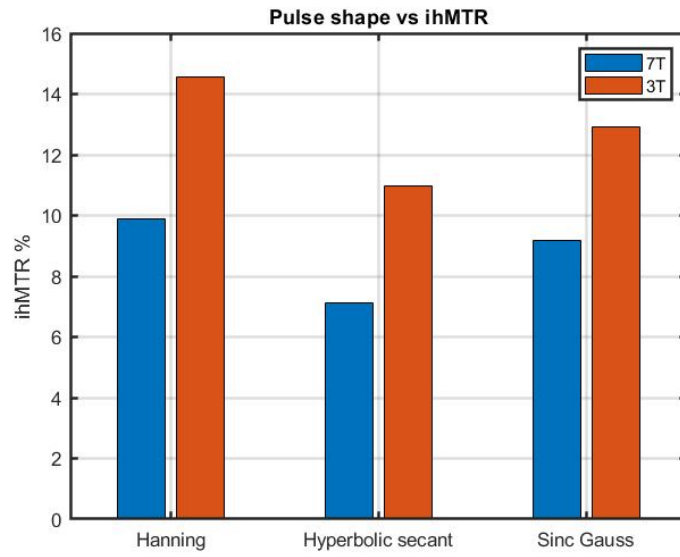


Figure A.4: Pulse shapes vs ihMTR for 3T vs 7T

away from water frequency and B_1 of $18\mu\text{T}$ strength with TR set to 150 ms.